Tailoring the modal structure of bright squeezed vacuum states of light via selective amplification

Samuel Lemieux

A thesis submitted to the
Faculty of Graduate and Postdoctoral Studies
in partial fulfilment of the requirements for the
MSc degree in Physics

Under the supervision of
Robert W. Boyd

Department of Physics
Faculty of Science
University of Ottawa

Abstract

The bright squeezed vacuum state of light is a macroscopic nonclassical state found at the output of a strongly pumped unseeded travelling-wave optical parametric amplifier. It has been applied to quantum imaging, quantum communication, and phase supersensitivity, to name a few. Bright squeezed states are in general highly multimode, while most applications require a single mode. We separated two nonlinear crystals in the direction of propagation of the pump in order to narrow the angular spectrum down to a nearly-single angular mode. We observed noise reduction in the photon number difference between the two down-converted channels, which constitutes of proof of nonclassicality. By introducing a dispersive medium between the two nonlinear crystals, we were able to tailor the frequency spectrum of bright squeezed vacuum and to dramatically reduce the number of frequency modes down to 1.82 ± 0.02, bringing us closer to truly single-mode bright squeezed vacuum.

Contents

1 Introduction **1**
1.1 Summary 1
1.2 Context and significance 3

2 Theory: squeezed vacuum and parametric amplification **7**
2.1 Quantization of the electromagnetic field: useful concepts and definitions 7
2.2 Quantum states of light: squeezed vacuum 9
2.3 Parametric down-conversion: a source of squeezed vacuum . . 11
2.4 Joint spectral amplitude 14
2.5 High-gain regime, Schmidt mode decomposition and entanglement 19
2.6 Birefingence and anisotropy: introducing the two-crystal configuration 26
2.7 Interference effects from two separated amplifiers 27
2.8 Gaussian beam optics 29
2.9 Dispersion and chirp 30

3 Selective amplification of angular modes **32**
3.1 Principle of the crystal-separation method 32
3.2 Noise reduction factor 33
3.3 Experiment and methods 35
3.4 Results and analysis 38
3.5 Conclusion 42

4 Selective amplification of frequency modes **43**
4.1 Qualitative description of the source 43
4.2 Pump and PDC propagating in different media 45
4.3 Experiment and methods 47
4.4 Results and analysis 49
4.5 Conclusion 55

5 Conclusion **58**

1 Introduction

Quantum mechanics is often described as the science of the extremely small, as it typically predicts behaviours at the particle scale and involving small distances. It is indeed unusual to observe quantum effects at the macroscopic scale, as quantum effects require coherence between the wave functions assigned to the particles of the system. Quantum states of light are said to be macroscopic when quantum mechanical behaviours are observed in conjunction with a large number of photons. The passage from quantum states with low number of photons to macroscopic beams requires the development of novel criteria for nonclassicality, testing apparatuses, and theoretical models. Broadly, this thesis is devoted to the study of the features of macroscopic quantum states of light.

The most recognized property of squeezed states is noise below the shot-noise level in one of their quadratures [1,2]. A squeezed vacuum is a squeezed state whose expectation value of electric and magnetic field amplitudes is zero, despite containing a nonzero number of photons. A squeezed vacuum state of light is said to be bright when it contains a large number of photons per mode [3–6]. Bright squeezed vacuum (BSV) states of light thus contain a large set of photons displaying quantum mechanical features. BSV are attractive for various applications in quantum imaging [7,8], quantum metrology [9, 10] and nonlinear optics with a nonclassical pump [11, 12], to name a few. The brightest squeezed vacuum states are generated via parametric down-conversion (PDC) by using two optical parametric amplifiers (OPA) with the optical axis tilted in opposite directions to reduce anisotropy [13]. The squeezed vacuum states generated this way are inherently highly multimode in both time and space, meaning that the coherence time and area of the down-converted light are much smaller than the duration and size of the pulse that carries it, thereby washing out some of their useful properties and making them less attractive for most applications. The ultimate goal of the work presented in this thesis is to generate BSV in a single mode of the electromagnetic field.

1.1 Summary

In this thesis, a two-crystal configuration is used to reduce the number of modes in BSV. In the first experiment, described in chapter 3, the number of angular modes was reduced down to almost one by separating the two nonlinear crystals in the propagation direction of the pump beam. In the second experiment, described in chapter 4, a dispersive medium is introduced between the nonlinear crystals, resulting in a dramatic decrease in the number of frequency modes. Both designs are theoretically described

and experimentally tested. The theory, based on the Schmidt mode decomposition of the biphoton amplification process, will be covered in chapter 2.

Separating the crystals along the direction of the pump beam leads to a selective amplification of the angular modes, since the multimode PDC exhibits a much broader angular spectrum than the pump. Using this method, it was possible to reduce the number of angular modes down to 1.13 ± 0.06. For the selective amplification of frequency modes, we introduced a dispersive medium between the two nonlinear crystals: the PDC generated in the first crystal undergoes chirp; the frequency-time correlation of chirped PDC allows the selective amplification of narrowband PDC in the second crystal. The number of frequency modes is reduced from roughly a hundred to 1.82 ± 0.02, without the use of any external filter.

A nonlinear crystal can be thought of as a three-wave beamsplitter: two OPAs thus form a nonlinear interferometer, whose output depends on the phase acquired by the three channels [10, 14–16]. The configuration of the nonlinear interferometer, namely the path lengths of the different channels between the two crystals, can have a dramatic effect on the number of modes, and on the shape and width of the frequency and angular spectra. The effect of the parametric gain, a parameter that determines the intensity of the PDC and that is proportional to the electric field amplitude of the pump, on the number of modes is also addressed. Finally, in the case of the frequency-mode-selection experiment, varying the optical path length of the pump arm of the interferometer has the effect of selecting a narrowband nondegenerate spectrum out of the whole PDC spectrum of the first crystal.

Theoretical predictions are based on the recently developed Schmidt mode formalism for optical amplifiers, where the amplification process is decomposed into eigenmodes that can be considered as independent squeezers, and amplified separately as such [17–21]. This model provides information about the rich modal structure of PDC: the weight and the spectral shape of each mode are used to determine the degree of entanglement, the degree of intensity correlation, and the high-gain spectrum of PDC.

One of the signatures of squeezed vacuum states of light is that they possess an even number of photons. In the case of nondegenerate squeezed vacuum, the number of photons is equally split between the two channels. The fluctuations in the photon-number difference between the two channels are very much below the shot-noise level, with a theoretical boundary of zero. Such a measurement is a sufficient test for nonclassicality, and is a sign of so-called twin-beam squeezing [22]. Like most quantum effects, the noise reduction in the photon number difference is very sensitive to losses, and even more so in the macroscopic regime [3, 23]. In this thesis, squeezing

in the form of noise reduction is observed in bright nondegenerate down-converted light generated in a single angular mode. The use of an external filter, for instance a fiber to select a single angular mode, is likely to introduce losses and therefore be fatal for the quantum properties. Alternatively, some clever dispersion management techniques were developed in order to generate single-mode quantum states from PDC [24,25]. However, they cannot be extended to the entire transparency range of the nonlinear crystals, and often require waveguides, thereby limiting the maximum gain available.

1.2 Context and significance

The work presented in this thesis is part of a worldwide effort to test, understand, predict and apply the features of quantum states of light. In 1927, P.A.M. Dirac quantized the electromagnetic field following the lines of second quantization [26]. He found that the electromagnetic field modes behave just like the quantum harmonic oscillator: they have discrete energy levels separated by $\hbar\omega$, where ω is the angular frequency, and one could apply creation and annihilation operators on them, following the bosonic commutation rules. The photon was born. The birth of quantum optics is attributed to Roy Glauber who described in 1963 the quantized electromagnetic field in terms of coherent states and correlation functions [27, 28]. Quantum optics provided an explanation for phenomena like spontaneous emission—hitherto mysterious—and paved the way for many others that could not have been predicted by the semi-classical theory: squeezed states, Hong-Ou-Mandel coalescence, Einstein-Podolsky-Rosen pairs, etc. Quantum optics had and still has deep implications in fundamental and applied physics alike, in fields as diverse as coherence theory, matter-light interaction, quantum information, opto-mechanics and lasers, to name a few. This thesis will deal mostly with elements of coherence theory.

One of the weird signatures of quantum mechanics is *entanglement*. Two particles, for instance photons created via PDC, are said to be entangled when their state must be described as a whole. This kind of correlations brought along the Einstein-Podolsky-Rosen paradox, which later motivated the famous Bell's theorem, all in all challenging the very concepts of locality and realism of the universe [29].

There is more to entanglement than just paradoxical peculiarities.By exhibiting behaviours that could not be reproduced by classical particles, quantum particles turned out to be a fertile ground for applications. Entanglement could be used to perform teleportation, where the state of a particle is transferred to another particle, notwithstanding the distance between them (the current record being 143 km in free space [30]). Also, for the same

reason classical physics cannot predict the physics of quantum mechanics, classical computers cannot be used to adequately simulate the quantum-mechanical world. The idea of a quantum computer was popularized by Richard Feynman, who underlined the inability of classical computers to deal with the heavy calculations associated with wave function probability amplitudes, and thus their inadequacy to simulate quantum particles [31]. Later, Peter Shor found that a quantum computer could be used to break one of the most broadly used methods of encryption for secure communication, namely the factorization of a large number into two primes [32]. Finally, and as a last example out of many others, Artur Ekert discovered that entangled particles could be used to implement quantum cryptography protocols [33].

All these applications stimulated the development of an impressive variety of quantum related techniques and technologies, such as quantum memories, entanglement distillation, quantum logic gates, etc. Also, entanglement applications were extended from bipartite to multipartite entanglement, and from the binary variables (such as electron spin or photon polarization) to continuous variables (frequency, angles, intensity, etc) [34,35]. Of paramount importance was the development of cheap, robust and versatile sources of entangled particles. One such source is PDC, a coherent process in which two entangled photons are created from the annihilation of a more energetic photon (the *pump*) in an OPA, following the conservation of energy and momentum. The output of a travelling wave unseeded OPA is a squeezed vacuum state. Squeezed states were introduced in 1970 by David Stoler, who called them "minimum uncertainty packets" [36]. A remarkable series of publications by Horace Yuen and Jeffrey Shapiro described squeezed states as a tool for different quantum optics applications and provided techniques for generation and detection [37–39]. Carlton Caves made squeezed states even more mainstream by suggesting the use of squeezed vacuum to detect gravitational waves, thereby describing noise in an interferometer from quantum mechanical principles [40]. The next decades brought along a myriad of new ideas to enhance squeezed states applications and extend their scope, as well as models to describe them. It was only in 1985 that Richard Elliot Slusher *et al.* observed squeezing for the first time, from four-wave mixing [41]. Although the prediction and first observation of PDC dates back to the 1960's, squeezing from PDC was only observed in 1986 [42]. The detection of squeezing required the use of an indirect phase-dependent detection method, namely homodyne detection, where the field under scrutiny is mixed with a coherent field whose phase can be varied. This method is still widely used to this day, to measure not only the quadrature noise in squeezed states, but also to perform the full quantum state tomography [43].

Generation and detection of light is often a challenge in quantum optics

since most experiments deal with a low number of photons. In the experiments presented in this thesis, the states of light contain a large number of photons, allowing for direct detection. The advent of direct detection in quantum optics was made possible by the recent development of low-noise charge integrating detectors based on p-i-n diodes [44]. These detectors can have a wide dynamic range in the number of photons, up to 10^6 per pulse and beyond, and exhibiting an electronic noise as low as several hundred of photoelectrons. This method allows the detection of a large number of photons with an accuracy below the shot-noise level. Direct detection can thus be used to compare the photon-number difference in two-color PDC with a classical bound, establishing a simple test for nonclassicality to be described in details in section 3.2.

This thesis focuses on the generation of single-mode BSV, but the theoretical framework, the experimental techniques, and the conclusions could be of high relevance in broader quantum information of quantum metrology applications. For instance, parametric-amplification eigenmodes provided by the Schmidt mode formalism could be used as a basis for multivariate quantum information applications: the rich modal structure of PDC is yet to be harnessed.

Contribution of the author and aknowledgement

This thesis presents the work of many scientists. This short section will contextualize my contribution to the different parts of this project.

Most of the theoretical framework was developed by Polina Sharapova, Olga Tikhonova and Maria Chekhova. Specifically, their work aimed to theoretically describe the transverse profile of high-gain PDC from the Schmidt mode decomposition of the biphoton field [21,45]. With their help, I adapted the formalism from the angles to the frequencies, and I used it to perform the different high-gain theoretical predictions throughout chapter 4.

The chapter 3, about the angular mode selection method, mainly consists of two experiments: selection of a single angular mode and measurement of twin-beam squeezing. The first experiment was done mostly by Angela Pérez, the second one by Timur Iskhakov and myself. The theory was provided by Polina Sharapova, Olga Tikhonova and Maria Chekhova.

My main contribution is the temporal mode selection method, described in chapter 4. I designed and set up this experiment under the guidance of Maria Chekhova, acquired almost all the data and calculated all the theoretical predictions presented in the chapter. Mathieu Manceau acquired some of the data. Timur Iskhakov and I worked on an earlier version of this

experiment [46].

This thesis was completed under the supervision of Robert W. Boyd, in the context of a collaboration with Gerd Leuchs and Maria Chekhova from the Max Planck Institute for the Science of Light in Erlangen, Germany. I would like to thank Maria Chekhova for her patience and dedication.

2 Theory: squeezed vacuum and parametric amplification

Squeezed states of light exhibit features that cannot be explained by classical physics, such as fluctuations below the shot-noise limit (SNL). A thorough quantum mechanical treatment is needed to achieve satisfying predictions. Such a treatment will be provided in the next sections, establishing the bases necessary to address the physics of bright squeezed vacuum states, and in order to explain their behavior, to benefit from their properties, and to enhance their capabilities.

The concept of the photon is quickly introduced from the salient features of the quantized electromagnetic field. The squeezed vacuum state is defined ad-hoc from the squeezing operator, and then described from a photon-number statistics point of view. Later on, it will be related to one of the physical processes that generates it, PDC, which is of paramount importance in the context of this thesis. Recent development in the description of the PDC process involve the introduction of amplification eigenmodes. Most of the novelty of the work presented in this thesis stems from this formalism: these modes contain all the information about the photon-number statistics of PDC, as well as the different spectral properties. The two-crystal configuration will be introduced and described mathematically. Finally, elements of Gaussian beam optics and dispersion are provided.

2.1 Quantization of the electromagnetic field: useful concepts and definitions

The electromagnetic (EM) field can be separated into normal (or uncoupled) *modes*. Although non physical, polarized monochromatic planewaves typically appear in this kind of procedure as a convenient mathematical tool. The quantization of the EM field, as its name suggests, concludes that the energy in a mode is quantized and that each energy level is separated by $\Delta E = \hbar\omega$, commonly referred to as the energy of a *photon*. A photon is thus an energy packet corresponding to a mode of the EM field. Photons are bosons because their spin angular momentum has a magnitude of 1. Most of the definitions in this section are taken or inspired from [47].

Each EM mode behaves like a quantum harmonic oscillator, and the same formalism can be applied directly. It is convenient to use creation and annihilation operators ($\hat{a}^\dagger$ and $\hat{a}$) in relation with the number of photons n and the number operator $\hat{n}$, in accordance with the following definitions and

properties:

$$\begin{gathered}\hat{a}^\dagger |n\rangle = \sqrt{n+1}\,|n+1\rangle\,, \\ \hat{a}\,|n\rangle = \sqrt{n}\,|n-1\rangle\,, \hat{a}\,|0\rangle = 0, \\ \hat{a}^\dagger\hat{a}\,|n\rangle = \hat{n}\,|n\rangle = n\,|n\rangle\,.\end{gathered} \tag{1}$$

The bosonic commutation relation for the creation and annihilation operators is simply

$$[\hat{a}, \hat{a}^\dagger] = \hat{a}\hat{a}^\dagger - \hat{a}^\dagger\hat{a} = 1. \tag{2}$$

Following the analogy with the quantum harmonic oscillator, the optical *quadratures* $X1$ and $X2$ are the equivalent of the position x and the momentum p. In their normalized operator form (definitions may vary):

$$\begin{gathered}\hat{X1} \equiv (\hat{a} + \hat{a}^\dagger)/\sqrt{2}, \\ \hat{X2} \equiv (\hat{a} - \hat{a}^\dagger)/\sqrt{2}i, \\ [\hat{X1}, \hat{X2}] = i.\end{gathered} \tag{3}$$

Hermitian operators such as the quadrature operators $\hat{X1}$ and $\hat{X2}$ as well as the number operator $\hat{n}$ correspond to *observables*, roughly meaning that they can be measured. Typically, homodyne detection is required to measure the quadratures' noise and mean value. Because $\hat{X1}$ and $\hat{X2}$ do not commute, they are tied to the Heisenberg uncertainty principle:

$$\langle \Delta X1^2 \rangle \langle \Delta X2^2 \rangle \geq \frac{\hbar^2}{4}, \tag{4}$$

where $\langle \Delta X^2 \rangle$ is meant as the variance of some observable $\hat{X}$.

The electric field in the mode j is often separated into two terms: the *positive frequency part* and the *negative frequency part*. In its quantized form,

$$\begin{aligned}\hat{\boldsymbol{E}}(\boldsymbol{r}, t) &= \hat{\boldsymbol{E}}^{(+)}(\boldsymbol{r}, t) + \hat{\boldsymbol{E}}^{(-)}(\boldsymbol{r}, t), \\ \hat{\boldsymbol{E}}^{(+)}(\boldsymbol{r}, t) &= i\sqrt{\frac{2\pi\hbar\omega_j}{V}}\boldsymbol{\epsilon_j} e^{i(\boldsymbol{k_j}\cdot\boldsymbol{r} - \omega_j t)}\hat{a}_j, \\ \hat{\boldsymbol{E}}^{(-)}(\boldsymbol{r}, t) &= -i\sqrt{\frac{2\pi\hbar\omega_j}{V}}\boldsymbol{\epsilon_j} e^{-i(\boldsymbol{k_j}\cdot\boldsymbol{r} - \omega_j t)}\hat{a}_j^\dagger,\end{aligned} \tag{5}$$

where $\boldsymbol{\epsilon}$ denotes the polarization and V is the volume. This electric field operator is thus the summation of a creation operator and an annihilation operator, each with a phase. This informs us that the positive and negative frequency electric field operators will evolve the same way creation/annihilation operators do. Most field quantization procedures are performed in a cavity of volume V, but V can in principle be any volume, including free space. When the field is integrated over a volume V to determine, say, the energy, the volume V cancels out.

2.2 Quantum states of light: squeezed vacuum

In this section, we examine some features of quantum states of light in order to determine the photon number statistics of squeezed vacuum states.

The most prominent feature of squeezed states of light is sub-shot noise fluctuations in one of the quadratures, at the expense of the other [48]. The function that maps the quantum state onto the phase space is the Wigner quasiprobability distribution. When represented in phase space, it appears as if the state has been *squeezed*, thus the name, adopting an elliptical shape. This form of squeezing is called *quadrature squeezing*, in contrast with *number-phase squeezing*. Single-mode squeezed states are produced under the influence of a time-evolution operator called the single-mode squeezing operator $\hat{S}(\zeta)$, whose characteristic feature is a quadratic combination of creation and annihilation operators:

$$\hat{S}(\zeta) = \exp\big[(\zeta\hat{a}^2 - \zeta^*\hat{a}^{\dagger 2})/2\big], \tag{6}$$

where ζ, the squeezing parameter, is complex [2]. Its phase determines the angle of the squeezing ellipse with respect to the quadrature axes. In the context of this thesis, the phase of ζ will be set to zero for clarity. This operator is called the single-mode squeezing operator because it operates on only one output mode, in constrast with the two-mode squeezing operator, which distinguishes two output modes: $\hat{a}^2$ would be replaced by $\hat{a}\hat{b}$, and so on.

A state evolves in time in accordance with the time-independent Hamiltonian of the interaction $\hat{H}$ such that

$$|\psi(t)\rangle = \mathrm{e}^{-i(\hat{H}/\hbar)t}\,|\psi(t=0)\rangle\,. \tag{7}$$

The Hamiltonian of the squeezing interaction can be found by simply comparing equations (6) and (7):

$$\hat{H} = i\frac{\zeta\hbar}{2t}\hat{a}^2 + \text{h.c.}, \tag{8}$$

where h.c. is the Hermitian conjugate. One can thus use the Heisenberg equation of motion and the commutation relation to find how $\hat{a}$ and $\hat{a}^\dagger$ evolve under the squeezing operator:

$$\begin{aligned} \dot{\hat{a}} &= \tfrac{i}{\hbar}[\hat{H}, \hat{a}] = -(\zeta^*/t)\hat{a}^\dagger, \\ \dot{\hat{a}}^\dagger &= \tfrac{i}{\hbar}[\hat{H}, \hat{a}^\dagger] = -(\zeta/t)\hat{a}, \end{aligned} \tag{9}$$

the solution of which is

$$\begin{aligned} \hat{a}(t) &= \hat{a}(0)\cosh\zeta - \hat{a}^\dagger(0)\sinh\zeta, \\ \hat{a}^\dagger(t) &= \hat{a}^\dagger(0)\cosh\zeta - \hat{a}(0)\sinh\zeta. \end{aligned} \tag{10}$$

This relation is known as a Bogolyubov transformation.

A squeezed vacuum state is created when the squeezing operator is applied to the vacuum $|0\rangle$. The average number of photons of squeezed vacuum is not zero, despite its name:

$$\langle n \rangle = \langle 0 | \, \hat{a}^\dagger(t)\hat{a}(t) \, |0\rangle = \sinh^2 \zeta. \tag{11}$$

The degree of second-order coherence, or normalized intensity correlation between the fields i and j, is defined as [28]

$$g_{ij}^{(2)}(t_i, t_j) = \frac{\langle \hat{a}_i^\dagger(t_i)\hat{a}_j^\dagger(t_j)\hat{a}_j(t_j)\hat{a}_i(t_i)\rangle}{\langle \hat{a}_i^\dagger(t_i)\hat{a}_i(t_i)\rangle\langle \hat{a}_j^\dagger(t_j)\hat{a}_j(t_j)\rangle}, \tag{12}$$

$g_{ij}^{(2)}(t_i, t_j)$ in the case $i = j$ is called intensity auto-correlation, whereas $i \neq j$ corresponds to intensity cross-correlation. The intensity autocorrelation is often expressed as $g^{(2)}(\tau = t_j - t_i)$, where the field overlaps itself with a temporal delay τ. $g^{(2)}(\tau)$ strongly depends on the state of light under scrutiny, and gives precious information about the field's photon number fluctuations [48]. For single-mode radiation, and when $\tau = 0$, the definition of $g^{(2)}(\tau)$ simplifies to:

$$g^{(2)}(\tau = 0) = \frac{\langle \hat{a}^\dagger \hat{a}^\dagger \hat{a}\hat{a}\rangle}{\langle \hat{a}^\dagger \hat{a}\rangle^2}. \tag{13}$$

where we dropped the time dependence of the creation and annihilation operators. For single-mode squeezed vacuum, using equation (10) we find

$$g^{(2)}(\tau = 0) = 3 + 1/\langle n \rangle. \tag{14}$$

In the case of two-mode squeezed vacuum, the same procedure can be applied to derive the photon-number statistics in each channel:

$$\langle n \rangle = \sinh^2 \zeta, \tag{15a}$$

$$g^{(2)}(\tau = 0) = 2. \tag{15b}$$

Finally, the intensity cross-correlation at zero delay between the two fields of two-mode squeezed vacuum is:

$$g^{(2)}(\tau = 0) = \frac{\langle \hat{a}^\dagger \hat{b}^\dagger \hat{b}\hat{a}\rangle}{\langle \hat{a}^\dagger \hat{a}\rangle\langle \hat{b}^\dagger \hat{b}\rangle}, \tag{16a}$$

$$g^{(2)}(\tau = 0) = 2 + 1/\langle n \rangle, \tag{16b}$$

where (16b) was found by applying the commutation relation on the creation and annihilation operators appearing in (16a). From (15b), we find that the fluctuations in each channel of two-mode squeezed vacuum follow thermal statistics. Likewise, from (16b), when the average number of photons is high, the cross-correlation also displays thermal fluctuations.

2.3 Parametric down-conversion: a source of squeezed vacuum

Parametric down-conversion (PDC) is a nonlinear three-wave mixing process commonly used to generate entangled photon pairs (figure 1). The three channels that interact in the nonlinear medium, or optical parametric amplifier (OPA), are typically labeled the pump, the signal and the idler, which will be denoted with the subscripts p, s and i respectively. Not explicit in the figure is the importance to consider the input state of the down-converted channels, even if it is vacuum. The output of a pumped unseeded OPA is squeezed vacuum in the signal and idler channels. In this section, we will examine the PDC process, and relate it to squeezed vacuum states of light. Most of the elements of nonlinear optics are from [49].

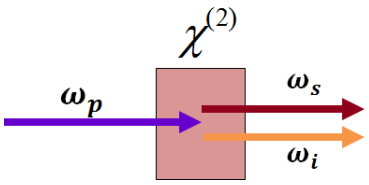

Figure 1: Parametric down-conversion is a three-wave mixing process occuring in a material exhibiting nonlinear susceptibility $\chi^{(2)}$, where the energy of the pump p is split into the down-converted channels, namely the signal s and the idler i.

Two conditions are required to generate PDC light: energy conservation and phase matching. Using the photon picture, the mathematical formulation of the energy conservation criterion is straightforward: $\hbar\omega_p = \hbar\omega_s + \hbar\omega_i$, where ω is the angular frequency. Phase matching implies that the oscillatory contributions to the amplitudes from different parts of the medium add up constructively. There is perfect phase matching when the wave mismatch $|\boldsymbol{\Delta k}| = |\boldsymbol{k_p} - \boldsymbol{k_s} - \boldsymbol{k_i}| = 0$. $\boldsymbol{k_x}$ is a wavevector of magnitude $k = 2\pi n(\lambda_x)/\lambda$, where λ_x is the wavelength in vacuum.

Birefringent crystals are often used in nonlinear processes in order to fulfill the phase-matching condition. Barium borate (BBO) in the β phase is a common nonlinear optical material that possesses a high nonlinearity and a wide transparency range in wavelength. Uniaxial birefringent materials such as BBO exhibit two refractive indices for every wavelength, labeled *ordinary* and *extraordinary*, and defined with respect to the *optic axis*, which corresponds to the direction perpendicular to the cristallographic planes. Light whose polarization is perpendicular to the optic axis undergoes the ordinary refractive index: this polarization, which lies in an isotropic crystallographic plane, is called the ordinary ray. Alternatively, light whose polarization is collinear or partially collinear with the the optic axis is governed by the

extraordinary refractive index; this light, called the extraordinary ray, *sees* the anisotropy, and its effective refractive index will depend on the angle between its polarization and the optic axis. The refractive index of the extraordinary ray lies between the ordinary and the extraordinary refractive indices, following the index ellipsoid [49, 50]. This versatility in the refractive index of the extraordinary ray is the key to enable phase matching in nonlinear birefringent crystals.

The phase-matching condition is fulfilled when $|\boldsymbol{\Delta k}| = 0$. In the case of collinear (same direction of propagation) and degenerate ($\omega_s = \omega_i = \omega_p/2$) PDC, the phase-matching condition requires $n(\lambda_p)/\lambda_p = n(\lambda_s)/\lambda_s + n(\lambda_i)/\lambda_i$, or, simply, $n(\lambda_p) = (n(\lambda_s) + n(\lambda_i))/2$. From the dispersion relation of BBO, shown on figure 2, we can see that phase-matching can occur for $\lambda_p = 400\,\text{nm}$ and $\lambda_s = \lambda_i = 800\,\text{nm}$ if the down-converted channels are set to ordinary (o), the pump to extraordinary (e), and by tuning the angle between the pump polarization and the optic axis of the crystal. This situation is called type-I phase-matching, characterized by the following relations between different channels and their polarization: pump-e, signal-o, idler-o. Alternatively, type-II phase-matching takes the form: pump-e, signal-o, idler-e, or pump-e, signal-e, idler-o.

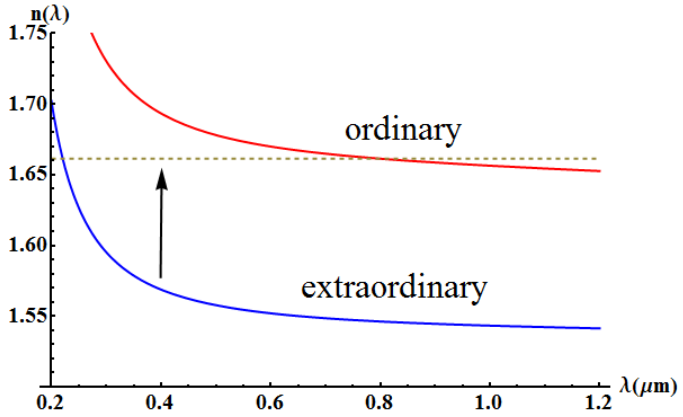

Figure 2: Dispersion relation of BBO for the ordinary and the extraordinary refractive indices [51]. The refractive index of the extraordinary ray can be set anywhere between the two curves. The dashed line shows the value of the ordinary refractive index at 800 nm. For type-I phase matching with degenerate PDC at 800 nm, the refractive index of the extraordinary ray should intercept the dashed line at 400 nm, following the black arrow.

In the PDC process, roughly stated, one pump photon is split into two photons: the signal and the idler. Already, a similarity appears with the squeezing operator of equation (6) or the interaction Hamiltonian of equation (8): photons are created or annihilated in pairs. A mathematical description

of the three-wave mixing process will push the similarity further and provide an insight about the nature of the squeezing parameter ζ. Assuming a constant strong pump field in the OPA and the slowly varying envelope approximation, the dependence of the classical field amplitudes A_s and A_i, obtained from Maxwell's equations, on the propagation distance z is given by a couple of differential equations:

$$\begin{aligned} \frac{dA_s}{dz} &= \frac{i\omega_s^2\chi^{(2)}}{k_s c^2} A_p A_i^* e^{i\Delta k z}, \\ \frac{dA_i}{dz} &= \frac{i\omega_i^2\chi^{(2)}}{k_i c^2} A_p A_s^* e^{i\Delta k z}, \end{aligned} \tag{17}$$

where $\chi^{(2)}$ is the effective nonlinear susceptibility of the OPA, c is the speed of light and A_p is the pump field amplitude [49]. Around phase matching ($\Delta k \approx 0$), these equations possess the solution

$$\begin{aligned} A_s(z) &= A_s(0)\cosh r + A_i^*(0)\sinh r, \\ A_i(z) &= A_i(0)\cosh r + A_s^*(0)\sinh r, \end{aligned} \tag{18}$$

where

$$r \approx \frac{\chi^{(2)}\ n(\omega_p/2)\ \omega_p\,|A_3|\,z}{2c}. \tag{19}$$

We are interested in the quantum properties of the signal and the idler. By quantizing their fields (replacing the field amplitude by the creation or annihilation operators), and assuming a classical pump (parametric approximation), we end up with the transformation of these operators upon propagation in the OPA of length L:

$$\begin{aligned} \hat{a}_s(L) &= \hat{a}_s(0)\cosh r + \hat{a}_i^\dagger(0)\sinh r, \\ \hat{a}_i(L) &= \hat{a}_i(0)\cosh r + \hat{a}_s^\dagger(0)\sinh r. \end{aligned} \tag{20}$$

If the signal and the idler are degenerate and collinear, we can just rewrite equation (17) by removing s and i:

$$\frac{dA}{dz} = \frac{i\omega^2\chi^{(2)}}{kc^2} A_p A^* e^{i\Delta k z}, \tag{21}$$

whose solution is, under the same conditions as before and in the quantized form:

$$\hat{a}(L) = \hat{a}(0)\cosh r - \hat{a}^\dagger(0)\sinh r. \tag{22}$$

The operator $\hat{a}(L)$ of equation (22) turns out to be identical to the creation operator after the single-mode squeezing operator with squeezing parameter ζ of equation (10). Alternatively, the creation operators of equation (20) have the same form as those under a two-mode squeezing operator. Therefore, the squeezing parameter ζ is actually identical to r.

We found in equation (11) that the average number of photons in squeezed vacuum states increases exponentially with the squeezing parameter ζ. Because there is amplification, this parameter is often called the *parametric gain* and is labelled G. The parametric gain is proportional to the medium's nonlinear susceptibility, to the pump field amplitude and to the length of the medium, as per equation (19).

2.4 Joint spectral amplitude

In a PDC process, photons are created in pairs in a six-dimensional space comprising the frequency, the polar angle and the azimuthal angle of the signal and the idler[1]. There exists a probability amplitude, called the *joint spectral amplitude* (JSA), for each combination of these parameters. The JSA contains all the information about the frequency and angular spectra of PDC. In this section, we examine the JSA of PDC assuming collinear propagation (or zero polar angle for all channels), meaning that the 6-variable JSA reduces to a 2-variable JSA, depending only on the frequencies ω_s and ω_i. The same reasoning will in turn be applied to obtain the JSA in the angles. The derivation of the JSA for the angles was taken from [21].

The JSA is found from the interaction Hamiltonian of PDC

$$\hat{H} = -\int_V d^3\boldsymbol{r}\hat{\boldsymbol{P}}^{(\mathbf{2})}(\boldsymbol{r},t)\cdot\hat{\boldsymbol{E}}(\boldsymbol{r},t) \tag{23}$$

where $\hat{\boldsymbol{P}}^{(\mathbf{2})}(\boldsymbol{r},t)$ is the macroscopic nonlinear polarization operator for $\chi^{(2)}$ processes and $\hat{\boldsymbol{E}}(\boldsymbol{r},t)$ denotes the electric field operator; they are related through the nonlinear susceptibility of the material: $\hat{\boldsymbol{P}}^{(\mathbf{2})}(\boldsymbol{r},t) = \chi^{(2)}\hat{\boldsymbol{E}}(\boldsymbol{r},t)$ $\hat{\boldsymbol{E}}(\boldsymbol{r},t)$. The electric field is separated into its positive and negative frequency parts for the pump, the signal and the idler. Doing so, the scalar product of equation (23) yields numerous terms, but by keeping only the non-oscillatory terms, the Hamiltonian integral reduces to

$$\hat{H} = -\epsilon_0\int_V d^3\boldsymbol{r}\chi^{(2)}\hat{E}_p^{(+)}(\boldsymbol{r},t)\hat{E}_s^{(-)}(\boldsymbol{r},t)\hat{E}_i^{(-)}(\boldsymbol{r},t) + \text{h.c.}, \tag{24}$$

where we considered only one polarization. This integral can be solved by replacing the pump, signal and idler field operators with the definitions in equation (5). Assuming collinear propagation, conservation of the pump photon energy in the pair-generation process in the form of $\omega_p = \omega_s + \omega_i$, coherent pump with a Gaussian frequency profile and negligible anisotropy

[1] Wavevectors are often used in lieu of the angles.

due to walk-off in typical birefringent nonlinear media, we get

$$\begin{aligned}\hat{H} = i\hbar\Gamma \int_{\omega_s}\int_{\omega_i}\int_{z=0}^{L} d\omega_s d\omega_i dz \ \exp[i(k_p - k_s - k_i)z] \\ \times \exp\left[- \frac{(\omega_s + \omega_i - \overline{\omega}_p)^2}{4\Delta\omega_p^2}\right] \hat{a}^\dagger_{\omega_s}\hat{a}^\dagger_{\omega_i} + \text{h.c.},\end{aligned} \tag{25}$$

which can be integrated in the direction of propagation z for a nonlinear medium of length L:

$$\hat{H} = i\hbar\Gamma \int_{\omega_s}\int_{\omega_i} d\omega_s d\omega_i \ F(\omega_s, \omega_i)\hat{a}^\dagger_{\omega_s}\hat{a}^\dagger_{\omega_i} + \text{h.c.}, \tag{26a}$$

$$F(\omega_s, \omega_i) = \text{sinc}(\Delta k L/2) \ \exp\left[- \frac{(\omega_s + \omega_i - \overline{\omega}_p)^2}{4\Delta\omega_p^2}\right] \exp(i\Delta k L/2), \tag{26b}$$

where Γ is a coupling constant proportional to $\chi^{(2)}$, to the pump field amplitude and to the cross section of the pump profile; $F(\omega_s, \omega_i)$ is the joint spectral amplitude of PDC in a single nonlinear medium, assuming collinear propagation; $\Delta k = k_p(\omega_s + \omega_i) - k_s(\omega_s) - k_i(\omega_i)$ is the wave mismatch; $\overline{\omega}_p$ is the central wavelength of the pump and; $2\sqrt{2\ln 2}\Delta\omega_\text{p}$ is the full width at half maximum (FWHM) of the pump frequency spectrum in intensity. When the Schmidt modes' operators evolve in time, a coefficient proportional to Γt appears, where t is the duration of the interaction. This coefficient is the parametric gain G. The last factor of the JSA is just a phase that is often omitted.

The JSA depends only on the pump spectral profile and on phase-matching considerations, not on the parametric gain. In the low-gain regime ($G \ll 1$), the joint spectral intensity (JSI), defined as $|F(\omega_s, \omega_i)|^2$, corresponds to the probability density that the two photons are emitted at the frequencies ω_s and ω_i. The marginal distributions of the JSI correspond to the frequency spectra of the signal and the idler channel. In the high-gain regime, however, the number of photons per mode is not linear with the parametric gain, leading to distortions in the spectra. This issue will be addressed in the following sections.

If the pump is narrowband, a good estimate of the spectral width of PDC can be recovered without extensive calculations, simply by replacing the Gaussian pump profile by $\delta(\omega_s + \omega_i - \overline{\omega}_p)$. By doing so, the normalized frequency spectrum $\phi(\omega_s, \omega_i)$ reduces to

$$\phi(\omega_s, \omega_i) = \text{sinc}^2(\Delta k L/2), \tag{27}$$

where ω_s and ω_i are tied by the relation $\omega_s + \omega_i = \overline{\omega}_p$. Defining a central wavelength $\overline{\omega}_s$ for the signal and $\overline{\omega}_i$ for the idler, and a detuning Ω ($\Omega \ll$

$\overline{\omega}_{p,s,i}$) from perfect phase-matching, $\phi(\omega_s, \omega_i)$ becomes a function of Ω only. Starting with the Taylor expansion of k_s and k_i in Ω, around perfect phase matching:

$$\begin{aligned} k_s(\overline{\omega}_s + \Omega) &= k_s(\overline{\omega}_s) + k_s'(\overline{\omega}_s)\Omega + k_s''(\overline{\omega}_s)\Omega^2/2 + ... \\ k_i(\overline{\omega}_i - \Omega) &= k_i(\overline{\omega}_i) - k_i'(\overline{\omega}_i)\Omega + k_i''(\overline{\omega}_i)\Omega^2/2 + ... \end{aligned} \tag{28}$$

where the primes are derivatives with respect to Ω. The wave mismatch simplifies quite a bit:

$$\begin{aligned} \Delta k(\Omega) &= k_p(\overline{\omega}_p) - k_s(\overline{\omega}_s + \Omega) - k_i(\overline{\omega}_i - \Omega), \\ \Delta k(\Omega) &\approx \Omega\big[k_i'(\overline{\omega}_i) - k_s'(\overline{\omega}_s)\big] - \Omega^2/2\big[k_i''(\overline{\omega}_i) + k_s''(\overline{\omega}_s)\big]. \end{aligned} \tag{29}$$

In the two-color case ($\overline{\omega}_i \neq \overline{\omega}_s$), the term linear with Ω preponderates. In the case of degenerate type-I PDC, since the signal and the idler are indistinguishable, only the term quadratic in Ω remains. From the properties of the sinc function, the FWHM of this PDC frequency spectrum can be found:

$$\begin{aligned} \text{In the two-color case: FWHM} &= \frac{5.568}{L(k_i'(\overline{\omega}_i) - k_s'(\overline{\omega}_s))}, \\ \text{In the degenerate case: FWHM} &= 2\sqrt{\frac{2.784}{Lk''(\overline{\omega}_p/2)}}. \end{aligned} \tag{30}$$

In both cases, when the length of the crystal in increased, the FWHM decreases. Furthermore, both FWHMs depend on the dispersion of the nonlinear medium. The two-color width depends on the mismatch of k' (which happens to be the inverse of the group velocity) for the signal and the idler; the degenerate FWHM depends on the group velocity dispersion k''. For example, a 3-mm-thick β-BBO crystal angle-tuned for degenerate type-I phase-matching at 800 nm and a narrowband pump would give a spectral width of 36.17 THz, in units of $\omega/2\pi$. The relation between the spectral width, the length of the medium L, and the dispersion remains valid, qualitatively when the pump is not monochromatic. In practical terms, one might just increase the length of the nonlinear medium to narrow the frequency spectral width of PDC. However, this method, in addition to being costly, has its limits: if the medium is too long, anisotropy effects due to birefringence (see section 2.6) will corrupt the process and introduce unwanted features in the spectrum.

The JSA of a single crystal, described by equation (44), contains two factors. The first one is a sinc function that depends mostly on the nonlinear medium's properties and geometry, and it determines what frequencies are allowed by the phase-matching condition. The second factor is the pump's frequency profile: it determines which frequencies are allowed by the conservation of energy. The JSA of a fictitious nonlinear medium (to exaggerate

the features) is shown in figure 3, where the multiplication of the phase-matching factor and the energy conservation factor is made explicit[2].

Some features of the JSA are worth discussing. The phase-matching factor of figure 3a exhibits a curvature. This curvature is more pronounced (smaller radius) when the dispersion in the crystal is higher. The secondary maxima, arising from the sinc, are much weaker than the central peak (in figure 3d the secondary peaks are easier to see). Also, a thinner nonlinear medium gives a wider line (not explicit in figure 3a, but can be deduced from the argument of the sinc). The pump factor (figure 3b), or energy factor, goes as a straight line and corresponds to perfect anticorrelation between the two channels' frequencies. Finally, the JSA of figure 3c appears as a bounded structure, following the nonperfect overlap of the phase-matching factor and the pump energy factor.

The expression for the JSA in frequency discussed so far was obtained by requiring collinear propagation, meaning that the transverse wavevectors $\boldsymbol{q}_{s,i,p}$ are set to zero. This can be done experimentally by introducing a pinhole in the farfield. Alternatively, a simple expression for the JSA in the angles, or the transverse wave vectors $\boldsymbol{q}_{s,i}$, can be obtained by imposing a condition in the frequencies, $\omega_s = \omega_i = \omega_p/2$, which corresponds to the effect of a narrowband filter on the PDC field. The tranverse wave vectors JSA is found to have the form [21, 45]

$$F(\boldsymbol{q}_s, \boldsymbol{q}_i) = C \exp\left(- \frac{\sigma^2 |\boldsymbol{q}_s + \boldsymbol{q}_i|^2}{2} \right) \mathrm{sinc}\left(\frac{L|\boldsymbol{q}_s - \boldsymbol{q}_i|^2}{4k_p} \right) \exp\left(i \frac{L|\boldsymbol{q}_s - \boldsymbol{q}_i|^2}{4k_p} \right), \tag{31}$$

where C is a normalization constant, $2\sqrt{\ln 2}\sigma$ the FWHM of the pump waist intensity distribution, and k_p the norm of the pump wave vector. To obtain this function, a treatment similar to that of the JSA in frequency is used, assuming a large interaction volume with respect to the wavelength, but a thin crystal with respect to the inverse of the transverse wave vectors, expressed as $L \ll |q_{s,i}|^{-1}$. To write the JSA as a function of transverse wave vectors only, it is assumed that the transverse wave vectors are small compared to the longitudinal wave vectors, allowing one to use the paraxial approximation in the form of $\Delta k_z = (\boldsymbol{k}_p - \boldsymbol{k}_s - \boldsymbol{k}_i)_z \approx |\boldsymbol{q}_s - \boldsymbol{q}_i|^2/k_p$, where Δk_z is the longitudinal wave mismatch [52, 53]. An analogy can be made from the JSA of the frequencies: the Gaussian corresponds to the pump factor, and the sinc corresponds to the phase-matching factor.

[2]Note that the amplitudes should be multiplied, not the probability distributions. In the specific case of a single crystal, the two terms are real, so multiplying the probabilities directly yields the same result. When the radiation of more amplifiers is considered, the phase must be taken into account.

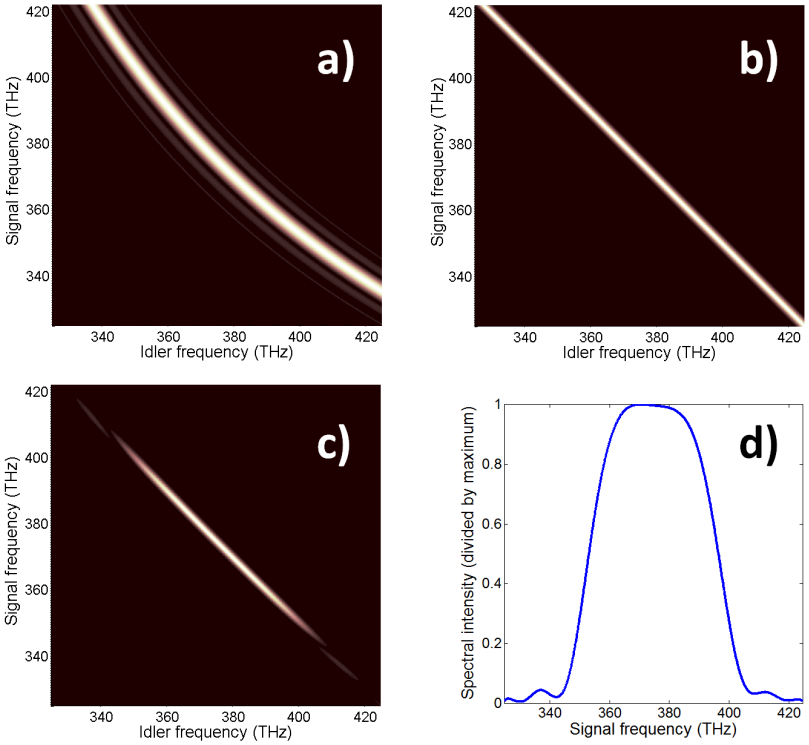

Figure 3: Features of the joint spectral amplitude of a single crystal of a fictitious nonlinear medium. a) Joint intensity distribution of the phase-matching factor. b) Joint intensity distribution of the energy conservation factor. c) Joint spectral intensity, obtained by multiplying the phase-matching factor (a) and the pump factor (b). d) Marginal intensity distribution of the joint spectral intensity, corresponding to the frequency spectrum of the PDC. For (a) to (c): Black is 0, and light pink is 1.

In this section, we described the joint spectrum of PDC, first in the frequencies, and then in the angles. In the literature, "biphoton amplitude" is often used instead of joint spectral amplitude. This denomination can be confusing, since this thesis is about PDC light with a large number of photons: in the high-gain regime, the generation of higher even number of photons is not negligible. Alternatively, the generation of photon pairs only, or biphotons, occurs only in the low-gain regime. In this case, the JSI (modulus square of the JSA) could simply be measured by coincidence detection, using two detectors with the appropriate narrowband filters. In the high-gain regime, however, the JSI does not provide an accurate description of the PDC spectra (in the angles or in the frequencies), since the different eigenmodes in the down-conversion process are not amplified equally. The mathematical description of PDC in the high-gain regime will be provided

in the following section.

2.5 High-gain regime, Schmidt mode decomposition and entanglement

By diagonalizing the Hamiltonian of the PDC interaction using the Schmidt mode decomposition, we can recover information about the level of entanglement, as well as describe PDC in the high-gain regime. We will show that the JSA directly describes the PDC in low-gain regime. We will then proceed to the mode decomposition of the downconverted light. Schmidt mode decomposition will be described first in frequency, and then briefly extended to the transverse wave vectors.

A state $|\Psi(t)\rangle$ evolving under a time-independent Hamiltonian can be found using the time-independent Schrödinger equation

$$i\hbar\frac{\partial}{\partial t}|\Psi(t)\rangle = \hat{H}|\Psi(t)\rangle\,, \tag{32}$$

which can be rewritten as

$$|\Psi(t)\rangle = \mathrm{e}^{(-it/\hbar)\hat{H}}|\Psi(t_0)\rangle\,, \tag{33}$$

where $|\Psi(t_0)\rangle$ is the input state, and $t > t_0$. In the low-gain regime, we make an approximation in the form of a Taylor expansion. Keeping only the first two terms, and with the vacuum as an input state, we get:

$$|\Psi(t)\rangle = \left(1 - \frac{it}{\hbar}\hat{H}\right)|0\rangle\,. \tag{34}$$

In the low-gain regime, the state is completely described by a superposition of the vacuum with a probability distribution of two-photon states given by the JSA. Thus, the JSA in the frequencies represents the joint probability amplitude to create a pair of photons with frequencies ω_s and ω_i.

In the high-gain regime, higher-order terms in the perturbative expansion (4-photon creation, 6-photon creation, etc.) cannot be neglected. One must solve the Heisenberg equation of motion for the creation/annihilation operators. Dropping the operator hats for clarity, the Heisenberg equation of motion reads

$$\dot{a}(\omega,t) = \frac{i}{\hbar}\big[H, a(\omega,t)\big], \tag{35}$$

where $a(\omega,t)$ denotes the annihilation operator in the mode ω after a time evolution of duration t. Introducing the expression of the Hamiltonian yields

$$\dot{a}(\omega,t) = i\hbar\Gamma\int d\omega_s \int d\omega_i F(\omega_s,\omega_i)\big[a(\omega,t), a^\dagger(\omega_s)a^\dagger(\omega_i)\big] \tag{36}$$

where

$$\big[a(\omega,t),a^\dagger(\omega_s)a^\dagger(\omega_i)\big]=\delta(\omega-\omega_s)a^\dagger(\omega_i)+\delta(\omega-\omega_i)a^\dagger(\omega_s). \tag{37}$$

The equation of motion thus reduces to

$$\dot{a}(\omega,t)=i\hbar\Gamma\bigg(\int d\omega_i F(\omega,\omega_i)a^\dagger(\omega_i)+\int d\omega_s F(\omega_s,\omega)a^\dagger(\omega_s)\bigg). \tag{38}$$

Equation (38) is a set of coupled integro-differential equation that cannot be solved analytically when written in this form. However, the Hamiltonian can be rewritten as a sum of independant Hamiltonians under the Schmidt mode decomposition of the joint spectral amplitude

$$F(\omega_s,\omega_i)=\sum_k \sqrt{\lambda_k}\ u_k(\omega_s)\ v_k(\omega_i), \tag{39}$$

where $\{u_k(\omega_s)\}$ is a set of orthogonal functions that describe the signal modes, $\{v_k(\omega_i)\}$ describe the idler, and where $\sum_k \lambda_k = 1$. The decomposed Hamiltonian thus reads

$$H=\sum_k H_k \tag{40}$$

where

$$H_k=i\hbar\sqrt{\lambda_k}\ \Gamma\int d\omega_s u_k(\omega_s)a^\dagger(\omega_s)\ \int d\omega_i v_k(\omega_i)a^\dagger(\omega_i)+\text{h.c.}. \tag{41}$$

This thus allows us to define a new set of broadband mode photon operators,

$$A_k^\dagger=\int d\omega_s u_k(\omega_s)a^\dagger(\omega_s),\quad B_k^\dagger=\int d\omega_i v_k(\omega_i)a^\dagger(\omega_i), \tag{42}$$

that follow, in general, the usual commutation relation

$$\big[A_j,A_k^\dagger\big]=\delta_{jk},\quad \big[A_j,B_k^\dagger\big]=0. \tag{43}$$

We are now interested to find the time-evolved Schmidt modes under the action of the newly formed Hamiltonian, again using the Heisenberg equation of motion:

$$\dot{A}_k=\frac{i}{\hbar}\big[H,A_k\big] \tag{44a}$$

$$\dot{A}_k=\frac{i}{\hbar}\big[H_k,A_k\big] \tag{44b}$$

$$\dot{A}_k=-\sqrt{\lambda_k}\ \Gamma\big[A_k^\dagger B_k^\dagger+B_kA_k,A_k\big] \tag{44c}$$

$$\dot{A}_k=-\sqrt{\lambda_k}\ \Gamma\big(\big[A_k^\dagger,A_k\big]B_k^\dagger+A_k^\dagger\big[B_k^\dagger,A_k\big]\big) \tag{44d}$$

$$\dot{A}_k=\sqrt{\lambda_k}\ \Gamma B_k^\dagger \tag{44e}$$

And similarly, it can be easily found that

$$\dot{B_k^\dagger} = \sqrt{\lambda_k}\ \Gamma A_k \tag{44f}$$

We can uncouple equations (44e) and (44f) by taking the time derivative of (44e), such as

$$\frac{d^2 A_k}{dt^2} = \sqrt{\lambda_k}\ \Gamma \frac{dB_k^\dagger}{dt} = \left(\sqrt{\lambda_k}\ \Gamma\right)^2 A_k \tag{45}$$

This differential equation describes a harmonic oscillator with frequency $\Omega = i\sqrt{\lambda_k}\Gamma$, whose general solution is

$$A_k(t) = \cos(\Omega t)\ C_1 + \sin(\Omega t)\ C_2. \tag{46}$$

The constants C_1 and C_2 are determined from the initial conditions

$$A_k(t=0) = C_1, \text{ and} \tag{47a}$$

$$\frac{dA_k(t)}{dt}\Big|_{t=0} = C_2\Omega, \text{ or} \tag{47b}$$

$$C_2 = \frac{\sqrt{\lambda_k}\ \Gamma}{\Omega} B_k^\dagger(t=0) = -iB_k^\dagger(t=0) \tag{47c}$$

Replacing Ω with its expression yields

$$A_k(t) = \cos\left(i\sqrt{\lambda_k}\Gamma t\right)\ C_1 + \sin\left(i\sqrt{\lambda_k}\Gamma t\right)\ C_2. \tag{48}$$

Using $\cos(ix) = \cosh(x)$ and $\sin(ix) = -i\sinh(x)$, we finally find

$$A_k(t) = \cosh\left(\sqrt{\lambda_k}\Gamma t\right)\ A_k(t=0) + \sinh\left(\sqrt{\lambda_k}\Gamma t\right)\ B_k^\dagger(t=0). \tag{49}$$

Parametric amplification from a short pump pulse can be seen as an interaction from $-\infty$ to ∞, but with an effective interaction time corresponding to the pump pulse duration τ_p [54]. The output photon operators thus read

$$A_k^{out} = \cosh(\sqrt{\lambda_k}G)\ A_k(t_0) + \sinh(\sqrt{\lambda_k}G)\ B_k^\dagger(t_0), \tag{50a}$$

$$A_k^{\dagger,out} = \cosh(\sqrt{\lambda_k}G)\ A_k^\dagger(t_0) + \sinh(\sqrt{\lambda_k}G)\ B_k(t_0), \tag{50b}$$

where $G = \Gamma\tau_p$, and t_0 is equivalent to $t = 0$. The average number of photons in mode k is

$$n_k^{out} = \langle A_k^{\dagger,out} A_k^{out}\rangle \tag{51a}$$

$$n_k^{out} = \sinh^2(\sqrt{\lambda_k}G). \tag{51b}$$

The downconversion spectrum, is obtained by summing the number of photons in all different Schmidt modes. The photon-number spectrum $N_s(\omega_s)$ for the signal is

$$N_s(\omega_s) = \sum_k n_k^{out}\ |u_k(\omega_s)|^2 = \sum_k \sinh^2(\sqrt{\lambda_k}G)\ |u_k(\omega_s)|^2, \tag{52}$$

and likewise for the idler photon. The photon-number spectrum is what would be measured by a photon-number resolving spectrometer averaged over a large number of pulses.

In general, the state given by (34) is entangled in the frequencies. It can be readily seen from a typical JSA shape, such as the one depicted in figure 3c, that the state described by the JSA is nonfactorable, or nonseparable, in the frequencies. In other words, knowledge about the signal photon frequency gives information about the idler photon frequency, and conversely. The signal and the idler channels are thus entangled in their frequencies, and all the information about the entanglement is contained in the JSA.

To quantify the entanglement in a nonseparable state, it is customary to express the whole state as a sum of factorable states, the so-called Schmidt modes, forming a complete set [17,18,55] of orthonormal functions. The degree of entanglement is simply obtained from the weight distribution of the Schmidt modes. Here, these modes correspond to the amplification eigenmodes in the nonlinear crystal. Each mode taken separately will exhibit the quantum statistical features of squeezed vacuum described in the previous sections, while a mixture of modes will not. Another physical meaning of Schmidt modes is pairwise correlation: a photon detected in a certain mode will undoubtedly have its twin in the corresponding Schmidt mode. Likewise, as we've seen, one can find the photon-number spectrum in the high-gain regime by finding the number of photons in each mode.

In the low-gain regime, the eigenvalues λ_k correspond to the relative weight of each mode, where the weight is defined as the ratio between the number of photon in a mode and the total number of photon. In the high-gain regime, however, because the number of photons is not linear with the product $\sqrt{\lambda_k}G$, the relative weight of modes with higher eigenvalues becomes increasingly more prominent. A simple normalization yields the actual relative weights $\tilde{\lambda}_k$:

$$\tilde{\lambda}_k = \frac{\sinh^2(G\sqrt{\lambda_k})}{\sum_{k=1}^{\infty} \sinh^2(G\sqrt{\lambda_k})}. \tag{53}$$

The number of modes is given by the Schmidt number K [18], using the normalized relative weights $\tilde{\lambda}_k$:

$$K = \frac{1}{\sum_k \tilde{\lambda}_k^2}. \tag{54}$$

Increasing the parametric gain, by increasing for instance the pump intensity, influences the PDC spectra in many ways (figure 4). Calculations show that when the gain of the first mode is set to 10, the width of the spectrum is reduced from 36.8 THz to 21.1 THz, and the number of Schmidt modes is brought down by a sizeable amount, from 62.9 to 11.7. The Schmidt mode decomposition of the Hamiltonian describing a single nonlinear crystal yields eigenfunctions like the ones of figure 4c. A higher-order Schmidt mode (higher k) will exhibit a broader spectrum, but a lower relative weight. The effect of the redistribution is explicit in figure 4b, where the first modes become obviously more prominent in the high-gain case. Finally, the incoherent sum of the different eigenfunctions, according to their respective width, yields predicted spectra like the ones in figure 4a. Note that a narrowing of the frequency spectrum from a single nonlinear crystal operated in the high-gain regime has yet to be demonstrated experimentally. More surprisingly, spectral broadening, instead of narrowing, has been reported [56]; this stumbling block remains to be addressed.

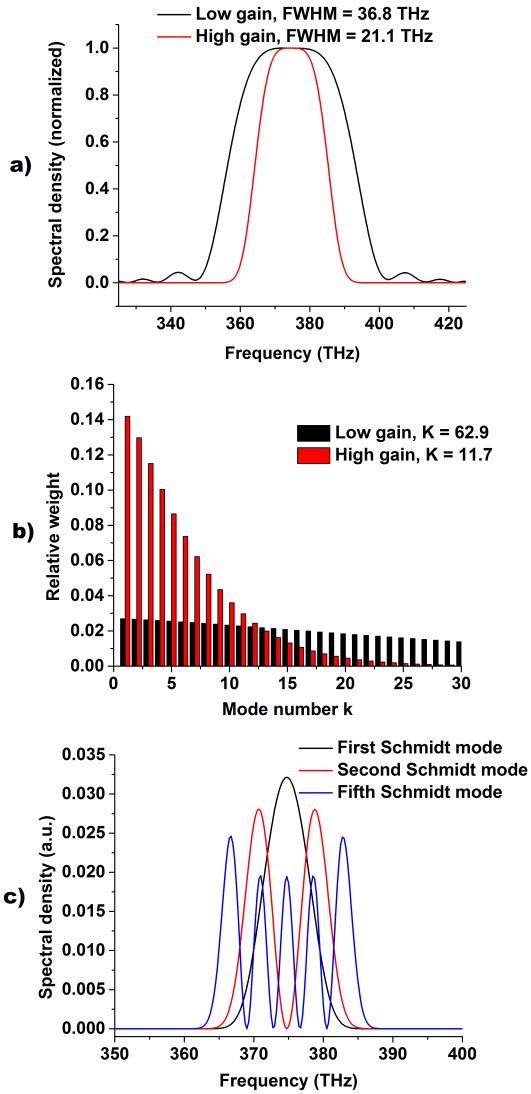

Figure 4: Example of a theoretically predicted comparison between low-gain and high-gain cases for a single BBO crystal aligned at degeneracy, pumped by a 0.9 ps pulse at 400 nm, obtained from equations (39), (53) *and* (54). *The high-gain case corresponds to a parametric gain of 10 for the first mode* ($G\sqrt{\lambda_1} = 10$). *a) Intensity spectrum, b) relative weight of each Schmidt mode, c) examples of several eigenfunctions (squared amplitude) corresponding to Schmidt modes.*

If our goal is to generate single-mode degenerate PDC, a possible strategy would be to increase the gain until the number of Schmidt modes is close to 1. For instance, a gain of 50 yields 3.41 modes, and a gain of 100, 2.09 modes. However, a parametric gain of 10 was optimistically high to begin with, and higher pump intensities are likely to damage some parts of the experimental setup. Another approach should be used, such as the

two-crystal configuration described in the following sections.

The two axes of the JSA ellipse (figure 3c) can be approximated as Gaussians (double-Gauss approximation) [18, 20, 21]. The eigenfunctions corresponding to Schmidt modes thus become Hermite functions, where the kth Schmidt mode corresponds to the $(k-1)$th Hermite-Gauss function, as in Fig. 2c. [17]. Additionally, the widths of the Schmidt modes are proportional to the geometric mean of the two axes of the "tilted ellipse" of the JSA. For instance, if the pump has a broader spectrum, or if the nonlinear crystal is thinner, the spectral width of the Schmidt modes will be broader.

The Schmidt mode decomposition can be applied as well to the 4-dimension angular spectrum of PDC, whose information is contained in the JSA for the transverse wave vectors $F(\mathbf{q}_s, \mathbf{q}_i)$, where $\mathbf{q}_{s,i}$ are the transverse wave vectors with magnitude $q_{s,i}$ and azimuthal angle $\phi_{s,i}$, and assuming $\omega_s = \omega_i = \overline{\omega}_p/2$ [21]. The Schmidt mode decomposition, mathematically equivalent to the singular value decomposition, cannot be performed directly on the JSA in this form, but the cylindrical symmetry of the PDC can be used to reexpress the angular JSA in another form. Explicitly, the JSA depends on the difference between the azimuthal angles $\phi_s - \phi_i$, whose periodic nature allows the JSA to be written as a Fourier series in the azimuthal angles [18, 52]

$$F(q_s, q_i, \phi_s - \phi_i) = \sum_n \chi_n(q_s, q_i) e^{in(\phi_s - \phi_i)}, \tag{55}$$

where $\chi_n(q_s, q_i)$, a function of the transverse wave vectors amplitudes, can be easily decomposed into the functions $u_{mn}(q_s)/\sqrt{q_s}$ and $v_{mn}(q_i)/\sqrt{q_i}$

$$\chi_n(q_s, q_i) = \sum_m \sqrt{\lambda_{mn}} \frac{u_{mn}(q_s)}{\sqrt{q_s}} \frac{v_{mn}(q_i)}{\sqrt{q_i}}. \tag{56}$$

The JSA can finally expressed in terms of Schmidt modes

$$F(\mathbf{q}_s, \mathbf{q}_i) = \sum_{m,n} \sqrt{\lambda_{mn}} \frac{u_{mn}(q_s)}{\sqrt{q_s}} \frac{v_{mn}(q_i)}{\sqrt{q_i}} e^{in(\phi_s - \phi_i)}, \tag{57}$$

where $u_{mn}(q_s)/\sqrt{q_s}$ are the Schmidt mode functions of the signal, and $v_{mn}(q_i)/\sqrt{q_i}$ the Schmidt mode functions of the idler. The integer n arose from the periodic nature of the azimuthal angles difference, and accounts for the orbital angular momentum of the mode it describes, and where the twin photon has the opposite charge. This angular mode decomposition can be used to calculate the angular spectrum of degenerate PDC in the high-gain regime, as well as the number of angular modes.

In this section, the JSA of the frequency spectrum of PDC was decomposed into Schmidt modes, assuming collinear propagation with the pump.

This decomposition allows one to amplify each mode separately and to predict the frequency spectrum in the high-gain regime. Alternatively, the JSA in the angles could be decomposed assuming $\omega_s = \omega_i = \overline{\omega}_p/2$. The angular space for biphotons has 4 variables, but the decomposition was performed on only two, making use of the intrinsic symmetries of the angular PDC field. To this day, the decomposition of the full PDC field (frequency and angles) was not demonstrated. From a quantum computation point of view, the Schmidt mode decomposition is a valuable tool to assess the number of modes, their shapes, the degree of entanglement and the entanglement entropy [18, 52, 55].

2.6 Birefingence and anisotropy: introducing the two-crystal configuration

A two-crystal configuration is often used to achieve high-gain PDC because it compensates for transverse walk-off effects. In this section, we examine some features of birefringence, its deleterious effects, and introduce some experimental methods used to mitigate them.

The frequency and angular spectra of PDC depend on the conservation of the pump photon energy and the phase mismatch between the signal, idler and pump channels. To achieve collinear PDC, where the three channels have a degenerate direction of propagation, the phase-matching condition $k_p - k_s - k_i = 0$ requires the use of a birefringent material. However, the k-vector and the Poynting vector do not have the same direction for the extraordinary ray. Since, for type-I phase matching, the pump is extraordinary, birefringence causes a transverse walk-off between the PDC generated at different positions along the material's length. The longer the crystal, the larger the transverse walk-off effect. Alternatively, if the pump is pulsed, the group-velocity mismatch between the PDC and the pump channels results in a longitudinal walk-off.

To generate high-gain PDC, it is critical to manage walk-off effects. In the general case, walk-off effects cause photons to be generated in different modes, so that the exponential amplification of the number of photons only partially takes place. It's not the length of the crystal that matters anymore, but the interaction time between the pump, the signal and the idler for a given mode of PDC. Using an arbitrarily long crystal to achieve higher amplication would thus be useless, without management of the walk-off effects.

The transverse walk-off can be mitigated by using a two-crystal configuration, where the optic axis of the second crystal is rotated 180° around an axis that corresponds to the polarization of the pump. The maximal transverse walk-off thus corresponds to the transverse walk-off of either crystal.

The same reasoning can be applied with more than two crystals, so that an arbitrarily long crystal length can be used without inducing additional transverse walk-off.

Longitudinal walk-off can in turn be mitigated by introducing slabs of dispersive material between nonlinear crystals [25, 57]. These slabs should exhibit dispersion opposite to that of the nonlinear crystal, so that the group-velocity mismatch is compensated in the long run. The maximum longitudinal walk-off thus correponds to the walk-off of only one of the nonlinear crystal slabs.

The use of more than one crystal can reduce the deleterious effects of birefringence, and is necessary to achieve high-gain PDC. Such a configuration constitutes a nonlinear interferometer where the nonlinear crystals act as nonlinear beamsplitters, splitting the energy between the pump, signal and idler modes, and where the output depends on the phase acquired by the different channels between the nonlinear crystals.

2.7 Interference effects from two separated amplifiers

A two-crystal configuration is a useful source of bright squeezed vacuum. In such a system, the deleterious effects of the anisotropy due to birefringence in the nonlinear media are mitigated by rotating the second amplifier. If the distance between the two crystals is zero, the JSA of the system corresponds to the JSA of an imaginary crystal with twice the length of an actual single crystal. Such a configuration will produce multi-mode PDC. This thesis describes the PDC generated in a two-crystal configuration, where the crystals are separated in the direction of propagation of the pump. The separated crystals constitute a source of quasi single-mode PDC in the angles. When a linear medium exhibiting strong group velocity dispersion is introduced between the crystals, the number of frequency modes is in turn dramatically reduced. In this section, the JSA of such a configuration is first derived for the frequencies, and the expression for the angles is provided afterwards.

To predict the frequency spectrum of PDC from two OPAs separated by a linear medium, one can start with the JSA of a single OPA, described in section 2.4. The collective JSA, with two crystals of length L and a linear dispersive medium of length L' betweem them, will be given by the coherent sum of the JSA of each crystal, based on the superposition principle

$$F(\omega_s, \omega_i) = F^{(1)}(\omega_s, \omega_i) + F^{(2)}(\omega_s, \omega_i), \tag{58}$$

where $F^{(m)}(\omega_s, \omega_i)$ corresponds to the JSA of the mth crystal, taken from a plane of reference in the propagation distance z, and taking the dispersion between the two crystals into account. Let us set $z = 0$ at the end of the

second nonlinear crystal. This way, $F^{(2)}(\omega_s, \omega_i)$ is obtained by integrating the phase functions of the signal, the idler and the pump in z over the thickness -L to 0. For the first crystal, however, the integration takes place from $-2L - L'$ to $-L - L'$, and phase is propagated through the linear dispersive medium, and through the second nonlinear crystal, as per

$$\begin{aligned} F^{(2)}(\omega_s, \omega_i) &= \int_{z=-L}^{0} dz\ e^{i\Delta k z}\ \exp\left[-\frac{(\omega_s + \omega_i - \overline{\omega}_p)^2}{4\Delta\omega_p^2} \right] \\ F^{(1)}(\omega_s, \omega_i) &= \int_{z=-2L-L'}^{-L-L'} dz\ e^{i\Delta k z}\ e^{-i[\Delta k' L' + \Delta k L]}\ \exp\left[-\frac{(\omega_s + \omega_i - \overline{\omega}_p)^2}{4\Delta\omega_p^2} \right], \end{aligned} \tag{59}$$

where $\Delta k = (k_p - k_s - k_i)$ is the wavevector mismatch in one of the crystals, and $\Delta k' = (k'_p - k'_s - k'_i)$ is the wavevector mismatch in the dispersive linear medium between the nonlinear crystals. Integrating (36) and summing the two JSAs, the collective JSA is found to have the form:

$$F(\omega_s, \omega_i) = \frac{\sin(\delta/2)}{\delta/2}\ \cos[(\delta + \delta')/2]\, e^{-i(\delta+\delta'/2)}\ \exp\left[-\frac{(\omega_s + \omega_i - \overline{\omega}_p)^2}{4\Delta\omega_p^2} \right] \tag{60}$$

where $\delta = (k_p - k_s - k_i)L$ is the phase mismatch accumulated in one of the crystals of length L, δ' is the phase mismatch accumulated between the two crystals due to the linear medium. If the signal, the idler and the pump propagate in the same medium between the two crystals, the phase mismatch can be written as $\delta' = (k'_p - k'_s - k'_i)L'$, where k' is the wavevector in the linear medium of thickness L'. The first factor of equation (60) corresponds to the JSA of a single crystal; the second and third factors describe the interference between the photons generated in the two crystals, given some dispersion between them; and the fourth term conveys the conservation of the pump photon energy.

In the angles, assuming again perfect degeneracy ($\omega_s = \omega_i = \omega_p/2$), the collective JSA adopts a similar shape. Explicitly,

$$\begin{aligned} F(\boldsymbol{q}_s, \boldsymbol{q}_i) &= C\ \exp\left[-\frac{\sigma^2 |\boldsymbol{q}_s + \boldsymbol{q}_i|^2}{2} \right] \mathrm{sinc}\left(\frac{\alpha}{2} \right) \\ &\times \cos\left(\frac{\alpha + \alpha' + \delta'_{PM}}{2} \right)\ \exp\left[i \frac{2\alpha + \alpha' + \delta'_{PM}}{2} \right], \end{aligned} \tag{61}$$

where α and α' are the phase accumulated due to transverse wave vector mismatch in the nonlinear and linear medium, respectively. δ'_{PM} is the longitudinal phase mismatch in the linear medium when there is perfect phase matching in the transverse wave vectors of the nonlinear medium, $|\boldsymbol{q}_s + \boldsymbol{q}_i| = 0$ [21, 25]. This factor does not appear in the frequency JSA because it is contained implicitly in the δ' phase. In the case of an air layer of thickness L', $\delta'_{PM} = (2n_p^{air} - n_s^{air} - n_i^{air})\omega_s L'/2c$. As previously, C is a

normalization constant and σ denotes the pump waist. The accumulated phases are explicitly given by:

$$\alpha = \frac{L|\boldsymbol{q}_s - \boldsymbol{q}_i|^2}{2k_p},\ \alpha' = \frac{L'|\boldsymbol{q}'_s - \boldsymbol{q}'_i|^2}{2k'_p}. \tag{62}$$

The two collective JSAs (one for the frequencies, and one for the angles) described in this section possess a similar form: a pump factor, a single-crystal phase-matching factor (sinc) and an interference factor (cosine). The second crystal has the effect of introducing modulations in the envelope of the spectrum of a single crystal through the cosine factor. The linear medium can influence the frequency or angular spectrum in several ways. For instance, increasing the length of the linear medium makes the modulations more dense in the spectrum. Also, we have seen at section 2.4 that for degenerate PDC the phase mismatch grows quadratically with the frequencies: this causes the modulations to oscillate slowly around degeneracy, then faster and faster as the frequency detuning is increased.

The collective JSA does not depend on the intensity of the pump beam or the presence of any seed. The Schmidt mode decomposition can be applied to such a system to extract the amplification eigenmodes, to quantify the level of entanglement in the frequencies and to determine the shape of the frequency spectrum in the high-gain regime, as was described previously.

2.8 Gaussian beam optics

Under typical conditions, laser beams are well described by Gaussian beam optics. The Gaussian beam is a solution to the paraxial Helmholtz equation, and therefore constitutes a wave whose wavefront normals make small angles with the direction of propagation. Some features of the physical processes presented in this thesis require the language and definitions of Gaussian beam optics. Specifically, the waist and divergence of the pump beam, which is well described by a Gaussian beam, have a strong influence on the PDC spectrum. In this section, only the relevant aspects of Gaussian beam optics will be discussed. A more exhaustive description of Gaussian beams can be found in most optics books, such as [50].

A Gaussian beam is cylindrically symmetric. Its intensity $I(r, z)$ depends on the axial and radial position, z and r, following

$$I(r, z) = I_0 \left[\frac{W_0}{W(z)}\right] \exp\left[-\frac{2r^2}{W^2(z)}\right], \tag{63}$$

where $z = 0$ corresponds to the waist of the beam, or focus, $W(z)$ is the beam width at position z, W_0 is the width of the beam at the waist, and I_0

is the optical intensity at the center of the waist ($z = 0, r = 0$). Specifically, these parameters are related by

$$W(z) = W_0\sqrt{1 + \left(\frac{z}{z_0}\right)^2} \qquad W_0 = \sqrt{\frac{\lambda z_0}{\pi}} \tag{64}$$

where z_0, called the Rayleigh range, is defined as the axial length z from the waist for which the beam width reaches $\sqrt{2}W_0$. Following the properties of Gaussian functions, for a given value of z, the intensity $I(r, z)$ at a radius value of $r = W(z)$ decreases by a factor of $1/e^2$ with respect to the intensity at the axis $I(r = 0, z)$. When $z \gg z_0$, the width W(z) grows linearly with z, the divergence θ_0 is thus defined as the angle between the axis and $W(z)$, $\theta_0 = \lambda/\pi W_0$. The Gaussian beam's profile along its direction of propagation is shown in figure .

From the mathematical relation between W_0 and z_0 arises an important property of Gaussian beams: a tighter focus will diverge more. Nonlinear optical processes often need intense laser beams. A stronger intensity can be obtained by focusing a laser beam. The experiments presented in this work involve nonlinear crystals separated by distances as large as 14 cm; the separation distance between the two crystals should be kept under the Rayleigh range of the pump beam.

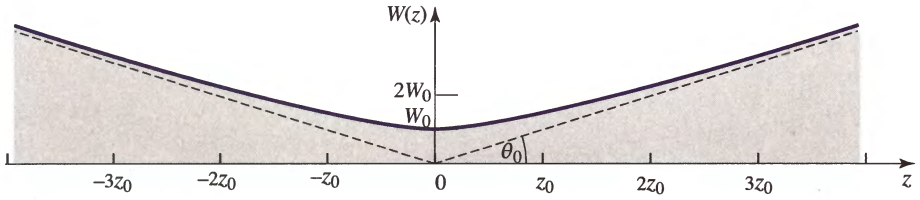

Figure 5: Radius of a Gaussian beam $W(z)$ along the direction of propagation z, around focus ($z = 0$). The beam width exhibits its minimum value W_0 at the beam waist, then reaches $\sqrt{2}W_0$ at the Rayleigh range $\pm z_0$. For large z, the width increases linearly with z, with divergence θ_0. From [50].

2.9 Dispersion and chirp

In wave mechanics, dispersion is the dependence of the refractive index on the frequency. The propagation of optical pulses is influenced by dispersion since pulses arise from the superposition of many frequencies. When the pump in a PDC process is pulsed, the PDC will also take the shape of pulse. The temporal mode selection experiment presented on Chapter 4 is based

on the spreading of PDC pulses, caused by group velocity dispersion. The effect of dispersion on optical pulses will be briefly reviewed.

Phase velocity, defined as $v(\omega) = c/n(\omega)$, where c is the velocity of light in vacuum, is the velocity of a monochromatic wave of frequency ω in a medium with the dispersion relation $n(\omega)$. Monochromatic waves with different frequencies, such as in a pulse, will propagate at different velocity, but the position of constructive interference, or the peak of the pulses's temporal envelope, will propagate at the *group velocity* u_g, defined as $u_g^{-1} = \frac{dk}{d\omega}\big|_{\omega_0}$, where ω_0 is the central frequency of the pulse, and $k = 2\pi n(\omega)$ is the wavenumber.

Group velocity itself depends on frequency, meaning that the different frequencies in a pulse spectrum propagate at different group velocities, and resulting in a temporal spread of the pulse. This phenomenon is called group velocity dispersion (GVD), and is closely related to $k'' = \frac{d^2k}{d\omega^2}\big|_{\omega_0}$. In this thesis, the quantity GVD associated to a dispersive material will be defined as GVD $= k''d$, where d is the thickness of the material, and which units are quadratic in time, typically fs^2 or ps^2. The dispersion is said to be normal when $k'' > 0$, and anomalous for $k'' < 0$.

Chirp, a frequency-time correlation in the pulse, is a phenomenon occuring as a result of GVD. When there is normal dispersion, the lower frequencies propagate faster, and thus end up at the front of the pulse, whereas the higher frequencies are slower and make up the tail; the opposite applies in the case of anomalous dispersion. When higher order dispersion effects are neglected, the instantaneous frequency $\omega(\tau)$ is linear with the time τ.

Most of the textbook theory of dispersion and chirp is based on Fourier transform-limited pulses, whose duration is the shortest considering its frequency spectral width. When the spectral width of some radiation is larger than the minimal width corresponding to its pulse duration, there is still group velocity dispersion and chirp, but on a scale that does not depend, for instance, on the original pulse duration, as is often the case in the theory.

3 Selective amplification of angular modes

PDC obtained at the output of an unseeded travelling-wave OPA is multi-mode squeezed vacuum, exhibiting a coherence area much smaller than its beam waist, as well as a pulse duration much longer than its coherence time. By strongly pumping two OPAs separated by a sufficient distance, it was possible to generate quasi-single-mode BSV in the angles (figure 6). This method makes use of the nonlinear amplification of modes that overlap the pump in the second OPA, making them significantly brighter with respect to the other ones. PDC generated in the two-color regime displays twin-beam squeezing. One of the salient features of twin beams is an identical number of photons in the two channels, resulting in a reduction of the noise in the photon number difference between the two channels below the shot-noise level (SNL) [3,4,23,58]. Just like many quantum effects, this behavior is very sensitive to losses, to the presence of stray light, and to imperfect alignment of the experimental setup, and even more so in the high-gain regime. At the same time, some of the possible applications of twin beams require single-mode radiation that still exhibits "squeezing", appreciated here through the noise reduction. The crystal-separation method was devised to generate BSV with single angular modes [45]. In this chapter, we will examine the effects of the crystal-separation method on the intensity of the PDC, on the number of modes and on the reduction of the noise.

3.1 Principle of the crystal-separation method

The generation of squeezed vacuum with a large number of photons is made possible by the addition of a second crystal, as described in section 2.6. The crystal-separation method was devised to reduce the number of angular modes of PDC, and ultimately to generate single-mode BSV. The principle of the method stems from the fact that PDC is generated in a cone broader than the divergence of the pump. The amplification takes place only for that solid angle of the PDC that overlaps the pump in the second crystal (figure 6). If the crystals of length L_c are separated by a sufficient distance L, so that the angular width of correlations of the PDC $\delta\theta$ is equal to the angle subtended by the PDC amplified in the second crystal, $\Delta\theta \approx a/L$, the source yields quasi single-mode radiation in the angles. $\delta\theta$ is the width of the $\theta_s = \theta_i$ diagonal of the JSA ellipse expressed in the angles, θ_s and θ_i. It determines the divergence of PDC. a is the diameter of the pump.

This method relies on the exponential amplification of the number of photons per mode: the modes that overlap the pump in the second crystal will interact over twice the distance as the non-overlapping modes. The exponential amplification is quantified with the parametric gain G, which is

proportional to the time of interaction between the pump and a mode. In the high-gain regime, when $G > 1$, the number of photons in the non-overlapped modes becomes negligible with respect to the number of photons in the doubly-amplified modes. G is typically extracted from the fit of a "Number of photons vs pump power" curve, based on the relation $\langle n \rangle = \sinh^2(G)$, where G is proportional to the square root of the pump power, and $\langle n \rangle$ is the average number of photons in a mode. G must be measured for a single mode, so the PDC should be properly filtered before detection.

To measure the number of angular modes, the PDC radiation is sent into a monochromator (for frequency filtering) and detected by a photon-number-resolving detector based on a charge integrating p-i-n diode. The number of angular modes is extracted from the intensity autocorrelation $g^{(2)}$ [59].

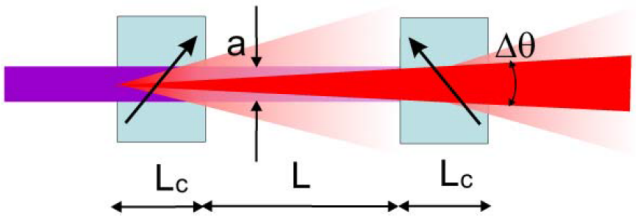

Figure 6: Principle of the crystals separation method. Only a small solid angle of the multimode PDC created in the first OPA overlaps with the pump in the second OPA, resulting in selective amplification. From [45].

3.2 Noise reduction factor

The reduction of the noise in the photon number difference, a nonclassical signature of two-color PDC, is assessed by the noise reduction factor (NRF), defined as:

$$\mathrm{NRF} \equiv \frac{\mathrm{Var}(\hat{n}_1 - \hat{n}_2)}{\langle \hat{n}_1 + \hat{n}_2 \rangle}, \tag{65}$$

where Var(X) and $\langle X \rangle$ are the variance and the expectation value of X; and where $\hat{n}_1$ and $\hat{n}_2$ are the photon number operators for channel 1 and channel 2. Already we see that if $\hat{n}_1$ and $\hat{n}_2$ are identical, the noise reduction factor goes to zero. Using the commutation relation of creation and annihilation operators, the variance in the photon number in a given field can be expressed in terms of $g^{(2)}$:

$$\begin{aligned} \mathrm{Var}(\hat{n}) &= \langle (\hat{a}^\dagger \hat{a})^2 \rangle - \langle \hat{a}^\dagger \hat{a} \rangle^2, \\ &= \langle \hat{a}^\dagger \hat{a}^\dagger \hat{a} \hat{a} \rangle + \langle \hat{n} \rangle - \langle \hat{n} \rangle^2, \\ &= g^{(2)} \langle \hat{n} \rangle^2 + \langle \hat{n} \rangle - \langle \hat{n} \rangle^2. \end{aligned} \tag{66}$$

The variance of the photon number difference between two fields with identical average photon number $\langle \hat{n}_1 \rangle = \langle \hat{n}_2 \rangle = \langle \hat{n} \rangle$ can thus readily be found as well in terms of intensity correlations [22]:

$$\begin{aligned} \mathrm{Var}(\hat{n}_1 - \hat{n}_2) &= \mathrm{Var}(\hat{n}_1) + \mathrm{Var}(\hat{n}_2) - 2\mathrm{Cov}(\hat{n}_1, \hat{n}_2), \\ &= \langle n \rangle^2 (g_{11}^{(2)} + g_{22}^{(2)} - 2g_{12}^{(2)}) + 2\langle \hat{n} \rangle, \end{aligned} \tag{67}$$

where $\mathrm{Cov}(X, Y) = \langle XY \rangle - \langle X \rangle \langle Y \rangle$ denotes the covariance between two variables X and Y. If follows, from the Cauchy-Schwarz inequality $\langle \hat{n}_1 \hat{n}_2 \rangle^2 \leq \langle \hat{n}_1^2 \rangle \langle \hat{n}_2^2 \rangle$, and from the algebraic fact that $\langle \hat{n}_1^2 \rangle \langle \hat{n}_2^2 \rangle \leq \frac{1}{4} \big(\langle \hat{n}_1^2 \rangle + \langle \hat{n}_2^2 \rangle \big)^2$, that $\langle \hat{n}_1 \hat{n}_2 \rangle \leq \frac{1}{2} \big(\langle \hat{n}_1^2 \rangle + \langle \hat{n}_2^2 \rangle \big)$. For classical fields, where the number of photons is not a quantum operator, the inequality can be rewritten in terms of intensity correlations, $g_{11}^{(2)} + g_{22}^{(2)} - 2g_{12}^{(2)} \geq 0$. Thus, again for classical fields, $\mathrm{Var}(\hat{n}_1 - \hat{n}_2) \geq 2\langle \hat{n} \rangle$, or NRF ≥ 1; a violation of this inequality is a sign of nonclassicality.

The NRF can be thought of as a measure of the noise in the photon number difference normalized on the average of the total number of photons, where the denominator can be corresponds to the minimal noise in the photon number difference for classical fields, namely the SNL. For instance, two uncorrelated coherent states, each with an average number of photons $\langle n \rangle$, will have a variance of the photon number difference $\mathrm{Var}(n_1 - n_2) = \mathrm{Var}(n_1) + \mathrm{Var}(n_2) = 2\langle n \rangle$, and the NRF is indeed equal to 1.

For squeezed vacuum, where $g_{11}^{(2)} = g_{22}^{(2)} = 2$, and where $g_{12}^{(2)} = 2 + 1/\langle n \rangle$, the NRF falls to zero. Even though fluctuations in the fields taken separately are considerable (thermal statistics), the number of photons is always identical. In other words, the two channels display perfect correlation in the photon number.

A direct measurement of NRF $= 0$ is not realistic with physical detectors. The best achievable NRF would rather be NRF $= 1 - \eta$, where η takes into account the efficiency of the detectors and losses in the optical system [3].

Like many quantum effects, the NRF is very sensitive to losses or imperfections in the alignment, such as clipping apertures, not perfectly circular irises, surfaces with unsufficient anti-reflection, etc. One of the approaches devised to reduce these deleterious effects is to introduce two circular apertures, one in each channel's path, and whose diameters are set by the transverse phase-matching condition:

$$\frac{D_i}{D_s} = \frac{\lambda_i^{max}}{\lambda_s^{min}}, \tag{68}$$

where D is the diameter of the aperture [3]. The max and min superscripts mean that the wavelengths should be chosen at the edge of their respective frequency spectra, and under the same criterion, in order to get the best photon-number matching.

A "mode" is sometimes loosely defined as a coherence volume of some radiation [5]. The number of modes in a pulse can roughly estimated by multiplying the number of transverse modes to the number of longitudinal modes in the pulse. The number of longitudinal modes is in turn estimated by taking the ratio between the pulse duration and the coherence time of the radiation; the number of transverse modes is found similarly from the diameter of the radiation and the coherence area. In a pair-generating process like PDC, and in the nondegenerate regime, each mode has a twin. When both modes in a couple reach their respective detector, they are said to be matched; when only one mode does reach its detector, this couple of modes is unmatched. A corrected estimation of the NRF has to take into account the number of matched modes m and unmatched modes k:

$$\mathrm{NRF} = 1 - \frac{m}{m+k}\eta + \frac{k}{m+k}\eta\langle n\rangle, \tag{69}$$

where $\langle n\rangle$ denotes the average number of photons per mode, $\langle n\rangle = \sinh^2(G)$, and G is the parametric gain [3]. This equation can be obtained from the definition of the NRF, equation (65), by supposing that k modes out of a total of $m + k$ are lost in one of the channels but not in the other. Thus, the appearance of $\langle n\rangle$ in the right-most term of equation (69) should come to no surprise: the numerator will have a term quadratic in $\langle n\rangle$, while the denominator will be linear. The consequence of equation (69) is that if there are more photons, the effect of unmatched modes will be more detrimental to the NRF. Thus, in the high-gain regime, where $\langle n\rangle$ is high, squeezing becomes extremely sensitive to misalignment and losses.

In some previous works, it was suggested that the parametric gain influences the "size" of the modes. For instance, Brida et al. observed an increase in the speckle size from a PDC radiation when the pump power was increased [58]. This behaviour can be readily explained by the Schmidt mode formalism, according to which it is the relative weights of the different modes that vary, not their size. Therefore, in the high-gain regime, fewer modes contribute, resulting in an increase in the coherence area of the PDC.

3.3 Experiment and methods

The experiment, illustrated in figure 7, consists of varying the distance between the OPAs and measuring: the intensity of the PDC; the intensity

autocorrelation with zero delay $g^{(2)}(0)$, which is used to extract the number of angular modes; and the spatial profile of the PDC with a camera. In a modified setup, to be described later, the NRF is measured as well.

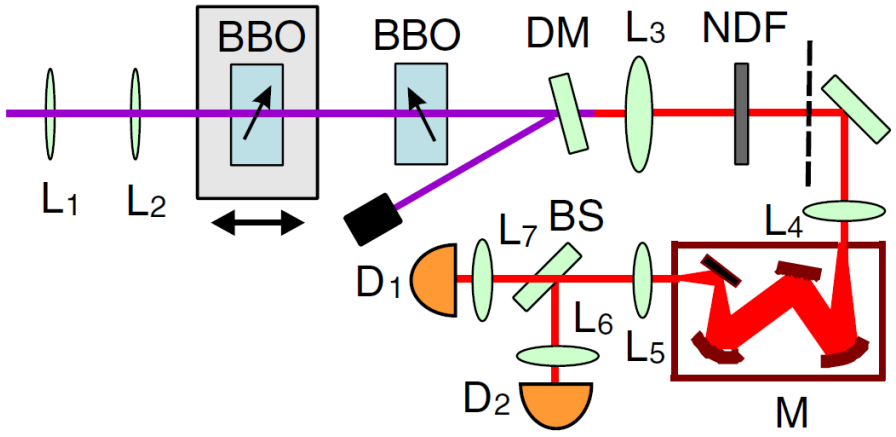

Figure 7: Experimental setup of the crystals separation method. A pulsed laser pumps PDC in two BBO crystals and is reflected out by a dichroic mirror (DM). The PDC is collimated (L_3), then focused ((L_4) into a monochromator (M) that brings down the number of frequency modes to 1.25. The PDC is then collected by the detectors to measure the intensity of PDC and $g^{(2)}(0)$. From [45].

The pump is the third harmonic of a Nd:YAG laser with a wavelength of 354.7 nm, pulse duration of 18 ps, repetition rate of 1 kHz, a mean power of 60 mW (60 μJ per pulse), and whose diameter is set to 200 μm (FWHM at the waist) with a telescope (L_1 and L_2). The pump is then directed through two BBO crystals, and removed from the setup with a dichroic mirror (DM).

The PDC from the crystals is collimated (L_3), then focused (L_4) into a monochromator (M, which selects a bandwidth of 0.1 nm corresponding to 1.25 temporal modes), and collimated again (L_5) to be collected by an intensity interferometer, consisting of a beam splitter (BS), two focusing lenses ($L_{6,7}$), and two p-i-n diode based charge-integrating detectors ($D_{1,2}$). The monochromator is purposefully set to 708 nm, close to degeneracy, but namely nondegenerate.

The two BBO crystals are 3 mm thick and cut for type-I degenerate collinear phase matching. The second one is rotated 180 degrees with respect to the first one, and around an axis that corresponds to the polarization of the pump beam, in order to reduce transverse walk-off, illustrated by the arrows in the crystals. The first crystal is mounted on a translation stage, allowing the separation between the crystals to vary from 7 to 170 mm.

To look at the spatial profile of the PDC, a CCD camera is introduced in the focal plane of L_3 (dashed line). The image on the camera corresponds to the angular profile directly, since it is located in the far field. Before detection from the camera, the PDC is filtered by an interference filter (not shown, transmission bandwidth of 10 nm around 710 nm). Finally, some neutral density filters (NDF) are used to avoid saturation of the camera and of the detectors.

The experimental number of modes is assessed from the degree of second-order coherence at zero delay τ,

$$g_m^{(2)}(\tau = 0) = 1 + \frac{\mathrm{g}_1^{(2)}(\tau = 0) - 1}{m}, \tag{70}$$

where m is the number of modes and $g_1^{(2)}$ the intensity autocorrelation one would expect from single-mode PDC [59]. From equation (16), in the case of single-mode nondegenerate collinear high-gain PDC, $g_1^{(2)} = 2$. $g^{(2)}$ is obtained experimentally from the definition $g^{(2)}(\tau = 0) = \langle{:}\hat{n}^2{:}\rangle / \langle\hat{n}\rangle^2 \approx \langle N^2\rangle / \langle N\rangle^2$, where the approximation is valid in the high-gain regime, and N in the intensity of the detected PDC. The number of angular modes m_a is extracted from the total number of modes m by using the approximation $m = m_a m_f$, where m_f, the number of frequency modes, was determined to be 1.25 [5].

Theoretical predictions are based on the Schmidt mode decomposition of the joint spectral amplitude of two separated crystals described in section 2.7. The number of modes is given by the high-gain Schmidt number (equation (54)), and $g^{(2)}$ is found from the number of modes, as per equation (70).

The NRF can be measured only if the signal and the idler channels can be separated. To do so, the BBO crystals are realigned for frequency nondegenerate phase matching ($\lambda_s = 635\,\mathrm{nm}$, $\lambda_i = 805\,\mathrm{nm}$, the monochromator, as well as the lenses L_3 and L_4 are removed, the beamsplitter replaced by a dichroic mirror. The angular spectrum of the PDC from a single crystal is rather large, whereas the spectrum from the two separated crystals is restricted. In the former case, it is necessary to introduce apertures in the signal and idler channels to reduce the deleterious effects of unmatched modes (asymmetric apertures, etc.); in the latter case, the effects of unmatched modes are mitigated by the narrow angular spectrum. Thus, in this experiment, no mode-matching apertures are used.

The detectors have a high quantum efficiency: 85% and 95% at 635 nm and 805 nm, respectively. The detection efficiency of the whole setup is

estimated to be 74%. The NRF is measured from the number of photons, which can be found from the amplification factor of the detectors. The amplification factor relates the number of photoelectrons at the input of a detector to the height of the voltage pulse at its output. It is determined from the fluctuations in the photon number difference of a Poissonian beam that went through a balanced beam splitter, which fall right on the shot-noise level [44, 60].

3.4 Results and analysis

When the distance between the two crystals is increased, the number of angular modes reduces, as illustrated by the increasing value of $g^{(2)}$ in figure 8. The highest value of $g^{(2)}$ is 1.71 ± 0.03, occuring at a distance of 11.5 cm between the two crystals, and correponding to 1.13 ± 0.06 angular modes. For this distance, 2.5×10^5 photons per pulse were detected, on average. A higher value of $g^{(2)}$ could not be achieved because the detectors collect a bit of the uncorrelated PDC from both crystals.

One of the striking features of figure 8 is the oscillations in both the PDC intensity and the intensity correlation. These oscillations appear to have a period of approximately 35 mm. The modulations in the signal can be explained by a slight dephasing between the pump, the signal and idler in air. Indeed, the phase mismatch acquired in a certain length of air L is given by $\Delta k\, L$, where $\Delta k = k_p - k_s - k_i$. By using the experimental values of wavelenghts, we find that a dephasing of 2π corresponds to an air thickness of 35.5 mm. The ocillations thus correspond to interference between the PDC generated in the first and the second crystal: constructive interference results in a stronger signal, whereas destructive interference yields a minimum. Modulations in $g^{(2)}$ can be explained from the same reasoning. When there is destructive interference, the amplification eigenmodes with the highest eigenvalues are not as prominent, with respect to the other modes, as in the case of constructive interference. The weights redistribution, due to the high gain, is thus less selective: the benefits of the high gain on $g^{(2)}$ are reduced because more modes are amplified less. From the theory, the oscillations are embodied by the cosine factor of the JSA. This factor depends on the thickness of the linear medium between the crystals, as per equation (61).

The angular intensity profiles are shown in figure 8 for the first two maxima in PDC intensity and the first minimum. The first maximum exhibits a ring pattern; the outer ring disappears in the second maximum; and the minumum shows a fainter donut profile. The disappearance of the outer ring in the second maximum is a demonstration of the mode selection tak-

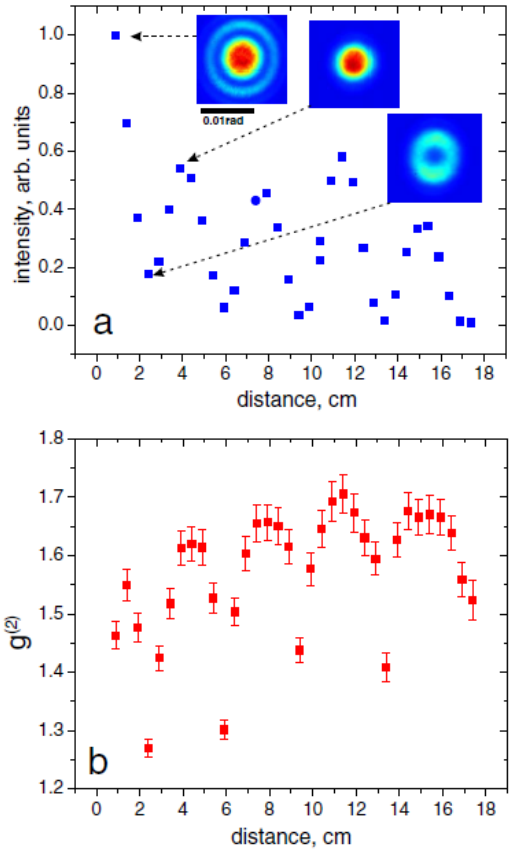

Figure 8: Dependence of the PDC intensity (a) and the normalized intensity correlation $g^{(2)}$ (b) on the distance between the crystals in a two-crystal configuration. The insets show the angular intensity profiles for different separation distances. From [45].

ing place in the crystals separation method. The effect of the interference between the crystals described in the last paragraph is straightforward from the intensity profiles: the maxima (minima) correspond to constructive (destructive) interference for the modes at the center of the angular distribution.

Theoretical predictions based on the amplification of squeezing eigenmodes are presented in figure 9. The curves exhibit strong similarities with experimental results. Mostly, the same oscillations due to interference appear, and the maximum value of $g^{(2)}$ occurs at the same separation distance, 11.5 cm. The estimated number of modes was taken into account while calculating $g^{(2)}$.

In theoretical predictions and experimental results alike, the values of $g^{(2)}$ corresponding to constructive interference do not grow monotonically

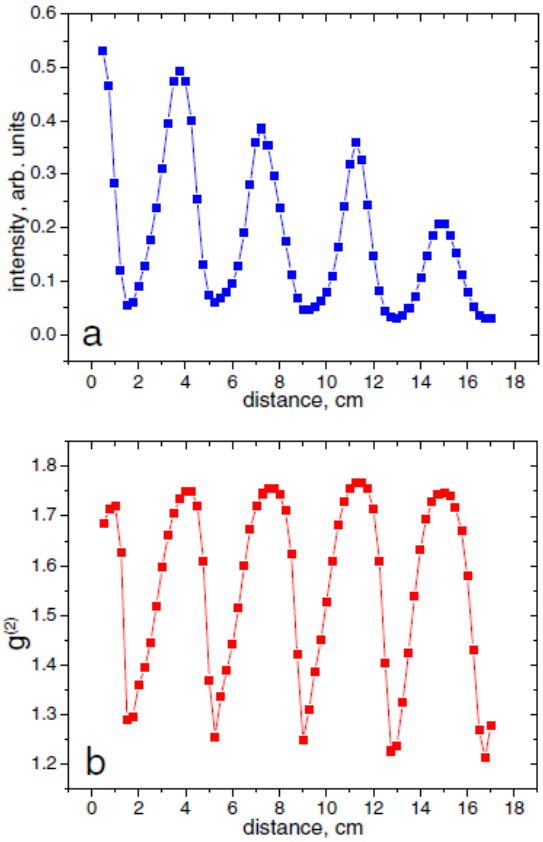

Figure 9: Theoretically predicted dependence of the PDC intensity (a) and intensity correlation $g^{(2)}$ (b) on the separation distance between the crystals, based on the eigenmode amplification. The lines were added for clarity. From [45].

with the separation distance. Rather, the maximum value of $g^{(2)}$ is found at 11.5 cm, and the next maximum yields a slightly lower value. This can be explained by a simple goemetrical argument. Intuitively, the separated crystals yield the highest value of $g^{(2)}$ when the PDC correlation angle $\delta\theta$, proportional to the pump's divergence, is equal to the angle of the PDC generated in the second crystal, $\Delta\theta$, approximately given by the ratio a/L (figure 6). If the crystals are separated further than that, then $\delta\theta > \Delta\theta$, and the amplification is not optimal anymore, leading to a decrease in $g^{(2)}$. Single-mode PDC in the angles occurs when $\delta\theta = \Delta\theta$, which is equivalent to $\lambda/a \propto a/L$. From this we can infer a simple scaling law that relates the separation distance L for single angular mode PDC, and the pump waist a: $L \propto a^2$.

NRF below the SNL was observed using the two-crystal configuration

(figure 10).The $g^{(2)}$ values are seen to behave in a fashion very similar to that of figure 8, but their values are much closer to unity because there was no frequency filtering, in order to preserve the level of squeezing. One can suppose that the maximum value of $g^{(2)}$ corresponds to single angular mode radiation with lots of frequency modes, and occurring again at a distance of 11.5 cm between the crystals.

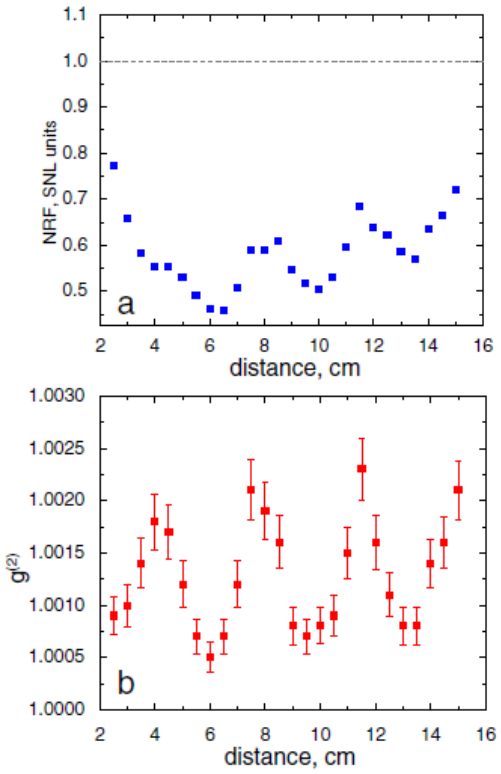

Figure 10: Dependence of the NRF (a) and intensity correlation (b) on the separation between the crystals. No mode-matching apertures were used. Dashed line is SNL. From [45].

The NRF oscillates with the separation distance following the $g^{(2)}$ curve and the PDC intensity (not shown). Following equation (69), a larger number of photons, in the presence of unmatched modes, translates to a larger NRF. Therefore, when the single angular mode selection is successful, the squeezing becomes more sensitive to the presence of unmatched modes. This behaviour can also be explained by a redistribution of the number of matched vs unmatched modes when the total number of modes is decreased. In our case, for single angular mode radiation at $L = 11.5$ cm, NRF $= 0.683 \pm 0.004$. This value should be compared with that of the ideal case (NRF $= 1 - \eta \approx 0.26$). This discrepancy can be explained from the fact

that mode-matching methods, such as introducing apertures in the setup, were not used.

3.5 Conclusion

The goal of these experiments was to observe reduction in the number of angular modes, as well as quantum features, from PDC generated with the crystals separation method. The number of modes was determined from the normalized intensity autocorrelation with zero delay $g^{(2)}(\tau = 0)$. Theoretical predictions were based on the Schmidt mode decomposition of the joint spectral amplitude, and on the nonlinear amplification of squeezing eigenmodes of the two-crystal scheme. The level of twin-beam squeezing is assessed through the reduction of the noise in the photon number difference between the signal and idler channels.

The number of angular modes was reduced down to 1.13 ± 0.06. The PDC generated in the other modes, although negligible, is not suppressed. This background PDC explains why the number of modes could not quite reach 1. It would be tempting to suppose that increasing the distance between the crystals would reduce further the number of modes, but we found that there exists an optimal separation distance, after which the number of modes starts increasing again. The optimal separation can be found from a scaling law, which depends only on the pump spatial width and the distance between the crystals.

The quasi single angular mode PDC from the two-crystal configuration exhibited fluctuations in the photon number difference lower than the shot-noise level, which is a sufficient criterion for nonclassicality. The noise reduction did not quite reach the ideal value, since the experiment was performed without using any mode-matching methods. Indeed, in the high-gain regime, the noise reduction is very sensitive to unmatched modes, in the form of imperfect alignment or apertures in the experimental setup. Still, the fact that twin-beam squeezing was observed without the use of mode-matching apertures is an impressive demonstration of the separated crystals method's angular selection power.

4 Selective amplification of frequency modes

According to the theory presented in section 2.5, in the high-gain regime, the nonlinear amplification of Schmidt modes causes a narrowing of the frequency spectrum, and a decrease in the number of modes. However, it was also discovered that a single nonlinear crystal, albeit very long or strongly pumped, will never quite produce single-frequency-mode PDC. A nonlinear interferometer consisting of two nonlinear crystals separated by a dispersive medium can be used to dramatically reduce the number of modes, both in angle and in frequency. The experiment described in this chapter focuses on the frequency spectrum and frequency modes.

In the angular case, described in the previous chapter, the selective amplification occurred because only part of the PDC generated in the first crystal overlapped the pump upon propagation through the second crystal. This is made possible because PDC generated in a travelling wave OPA exhibits an angular spectrum wider than the divergence of the pump. In other words, a smaller overlap in *space* resulted in a narrower angular spectrum. The experiment presented in this chapter is an analogy from the angular case, to be applied to frequencies, where, upon propagation in a dispersive medium, a smaller overlap in *time* of the pump and the PDC in the second crystal results in a narrower frequency spectrum.

Section 4.1 is a quick survey of the principle of the method in terms of group velocity dispersion (GVD) and parametric gain. The introduction of dispersion requires a separation of the pump from the PDC between the two crystals. Section 4.2 provides a mathematical description of the interferometer in order to adapt the expression for the joint spectral amplitude (JSA). In the following sections, the experiment is described, and the results are analyzed.

4.1 Qualitative description of the source

A nonlinear interferometer that consists of two nonlinear crystals and a medium exhibiting GVD in-between them is used to generate bright PDC and tailor its frequency spectrum (figure 11). A pump pulse is sent into the first OPA and generates a broadband PDC pulse. The latter is injected into the GVD medium and undergoes temporal spreading and chirp, meaning that the time and the frequency domains are henceforth correlated. In the second OPA, only the part of the stretched PDC that overlaps the unaltered pump pulse in the time domain is amplified. The second amplification is equivalent to selecting a narrower frequency width. No external frequency filter is used: the amplification is narrowband in and by itself.

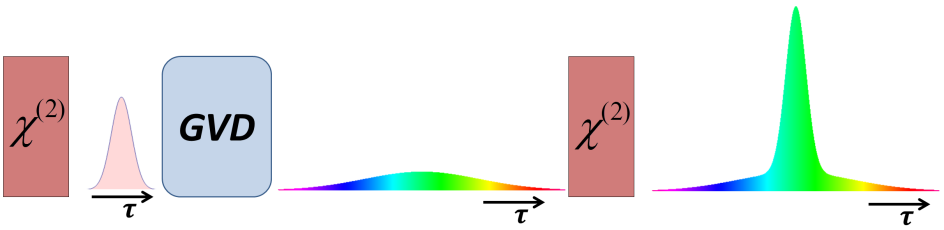

Figure 11: Principle of the method. A broadband PDC pulse is generated in an OPA; the PDC pulse experiences spreading and chirp after propagation in a medium exhibiting group velocity dispersion (GVD); the spread and chirped PDC pulse is amplified in another OPA, resulting in a selective amplification of the PDC from the first OPA. The shape of the pulse is shown in the temporal domain.

Parametric gain is a key concept behind this experiment. From the Bogolyubov transformation of the squeezing operator, we know that the average number of photons per mode is given by $\langle N \rangle = \sinh^2(G)$, where the parametric gain G is proportional to the pump's electric field amplitude, to the crystal's nonlinear susceptibility and, most importantly, to the length of the interaction with the pump pulse, which is usually the crystal length. In the high-gain regime—intense pump and high nonlinearity—, doubling the interaction length between the pump pulse and the PDC pulse increases the number of PDC photons by several orders of magnitudes. In our case, the interaction length is doubled only for the part of the stretched PDC pulse that overlaps the pump pulse in the second OPA, leading to a narrowband pulse.

The frequency spectral width and the number of modes will be used to assess the success of the method and to compare experimental results with theoretical predictions. Note that the number of modes is the ultimate measurement in order to claim single-mode PDC, as it provides information about the degree of entanglement between the signal and idler frequency spectra.

Following the intuition that the PDC pulse is chirped and stretched in time, it should follow that varying the time of arrival of the pump pulse tunes the frequency of the amplified PDC accordingly. This is performed simply by changing the length of the pump path. Furthermore, one would expect from conservation of the pump energy to see two peaks appearing on either side of the degenerate frequency. This instance will be labeled two-color or non-degenerate, as opposed to the degenerate case, where the PDC and pump pulses are synchronized so that there is only one peak at degeneracy.

4.2 Pump and PDC propagating in different media

In a two-crystal configuration separated by a linear dispersive medium, the PDC is described by the collective JSA. In frequency, this JSA is given by equation (60). This equation has to be reworked a bit since the pump and the PDC take up different paths between the two crystals. Specifically, the integral for $F^{(1)}(\omega_s, \omega_i)$, in equation (59), should explicitly contain the variables z_p, z_s and z_i, instead of just z, so that the pump, the signal and the idler propagate in their respective path. Conveniently, the collective JSA, described by equation (60) remains unchanged, but the expression for δ' gets substantially longer:

$$\delta' = \Phi_p - \Phi_s - \Phi_i, \text{ where the accumulated phase for each channel is}$$
$$\Phi_x = k_x^{(1)} L_x^{(1)} + k_x^{(2)} L_x^{(2)} + ... + k_x^{(m)} L_x^{(m)}. \tag{71}$$

m is the number of different media in channel x, $L_x^{(j)}$ is the length of the jth medium for the channel x, and the wavenumber is $k_x^{(j)} = \frac{2\pi\ n^{(j)}(\lambda_x)}{\lambda_x}$. Finally, $n^{(j)}(\lambda_x)$ is the refractive index of medium j for the wavelength of channel x.

Suppose that, between the two crystals, the PDC propagates through a 10 cm-thick slab of SF6 glass and 5 cm of air, so that $L_s^{air} = L_i^{air} = 5\,\text{cm}$ and $L_s^{SF6} = L_i^{SF6} = 10\,\text{cm}$. In this example. the pump only propagates through air, but we don't know the length of the air path yet. In the pulsed regime, the pump pulse should be synchronized with at least one of the PDC pulses upon propagation between the two crystals. In other words, the propagation times τ_p and $\tau_{\{s,i\}}$ must be equal, and one must make use of the group velocity $u_{g-x}^{(j)}$ in medium j for channel x. Let us suppose, as per our example, that we want to synchronize the pump pulse with the signal pulse:

$$\begin{aligned} \tau_p &= \tau_s, \\ \frac{L_p^{air}}{u_{g-p}^{air}} &= \frac{L_s^{air}}{u_{g-s}^{air}} + \frac{L_s^{SF6}}{u_{g-s}^{SF6}}, \\ L_p^{air} &= u_{g-p}^{air}\left(\frac{L_s^{air}}{u_{g-s}^{air}} + \frac{L_s^{SF6}}{u_{g-s}^{SF6}}\right). \end{aligned} \tag{72}$$

Equation (72) gives the length of air needed, in the pump path, to synchronize the time of arrival of the pump and signal pulses, for a given set of dispersive media in the PDC path.

By finding L_p^{air} using the synchronization of the pulses, equation (72) provides us with a valid configuration for a nonlinear interferometer that will produce PDC in the first crystal and amplify it in the second. However, the PDC amplitudes from the first and the second crystals will interfere. This

behavior is embodied by the cosine factor in equation (60), which takes into account the configuration of the whole interferometer through δ'. The probability amplitude for a combination of frequencies might drop to zero due to dispersion between the two crystals.

Suppose the crystals are aligned for phase matching aroung the frequencies $\overline{\omega}_s$ and $\overline{\omega}_i$. The cosine factor of equation (60) depends on L_p^{air}, which in turn depends on the media in the PDC arm through the synchronization condition. If the value of this cosine is ± 1 when $\omega_s = \overline{\omega}_s$ and $\omega_i = \overline{\omega}_i$, we get constructive interference. Otherwise, there is a more or less prominent hole in the center of the JSA.

Interference can have a profound effect on the spectrum and on the number of modes in the high-gain regime. When there destructive interference around degeneracy, it is reasonable to expect that the main Schmidt modes become prominent with respect to the other modes, enlarging the spectral width and increasing the number of modes via the Schmidt number K. Alternatively, it is reasonable to expect a narrower spectrum and fewer modes from constructive interference at degeneracy, when $\omega_s = \overline{\omega}_s$ and $\omega_i = \overline{\omega}_i$. To get constructive interference at the center of the JSA, two criteria must be fulfilled:

$$\begin{aligned} \text{Synchronisation of the pulses: } & \tau_p = \tau_{\{s,i\}}, \\ \text{Constructive interference: } & \cos[(\delta + \delta')/2] = \pm 1. \end{aligned} \tag{73}$$

These equations can be solved analytically. In our example, using the 10 cm of SF6 glass as a constraint, we wish to find the length of the air in the PDC path, and the length of the air in the pump path. In the specific case of crystals aligned for degenerate phase matching, so that s and i can be used equivalently, we get the following set of solutions:

$$\begin{gathered} L_s^{air} = \frac{u_{g-s}^{air}\big(- L_s^{SF6}\ n^{air}(\lambda_p)\ u_{g-p}^{air}\ +\ \lambda_p\ (i/2)\ u_{g-s}^{SF6}\ +\ L_s^{SF6}\ n^{SF6}(\lambda_s)\ u_{g-s}^{SF6}\big)}{\big(n^{air}(\lambda_p)\ u_{g-p}^{air}\ -\ n^{air}(\lambda_s)\ u_{g-s}^{air}\big)u_{g-s}^{SF6}}, \\ L_p^{air} = u_{g-p}^{air}\left(\frac{L_s^{air}}{u_{g-s}^{air}} + \frac{L_s^{SF6}}{u_{g-s}^{SF6}}\right), \\ where\ i = ... - 2,\ -1,\ 0,\ 1,\ 2... \end{gathered} \tag{74}$$

Using numerical values such as $\lambda_p = 400\,\text{nm}$ and the crystals aligned for PDC around 800 nm, we can get the following solutions for different values of i:

i	L_s^{air} (cm)	L_p^{air} (cm)
23913	9.3604	27.677
23914	8.1548	26.472
23915	6.9493	25.266
23916	5.7437	24.060
23917	4.5381	22.855

The PDC and the pump propagate in different media, so a solution of equation (74) will be very sensitive to phase fluctuations. For instance, if the air thickness in either channel undergoes a variation in the order of 100 nm, δ' goes from constructive to destructive interference. To achieve a precision of ~ 10 nm over lengths in the order of the meter is obviously rather challenging, and would furthermore require great stability.

4.3 Experiment and methods

The experimental setup (figure 12) consists of a nonlinear Michelson interferometer. The pump ($\lambda_p = 400$ nm) is the second harmonic of a Spectra Physics Spitfire Ace system with a 5 kHz repetition rate and 0.9 ps pulses; its power is measured right after an attenuator (half-wave plate and Glan polarizer); and its diameter is set with a telescope (f = 300 mm and f = -75 mm). A dichroic mirror (DM1, Newlight Photonics HS10-R400/T800) sends the pump towards a nonlinear crystal (β-BBO, type I degenerate collinear phase matching, 3 mm thick). Another dichroic mirror (DM2, same as DM1) reflects the pump while the PDC is transmitted. The pump is reflected by a mirror (M1) set on a translation stage to tune its time of arrival, while the PDC is sent into a dispersive medium (disp, various samples) and reflected back by a mirror (M2) into the dispersive medium again. The PDC and the pump are recombined at DM2. The PDC is amplified in the crystal in accordance with the time of arrival of the pump. After its transmision by DM1, the PDC can either be sent into a low-noise charge integrating detector based on p-i-n diode (PD) or reflected into the spectrometer by means of a flip mirror (flip). In the diode's arm, there is a variable attenuator (att) in case of saturation, a 500 μm pinhole to select a single angular mode, a longpass filter (LP1) and a focusing lens (f = 40 mm). The p-i-n diode is used to measure the signal intensity and $g^{(2)}$. The spectrometer arm consists of a longpass filter (LP2) and a focusing lens (f = 100 mm) to couple light into the spectrometer (Ocean Optics HR4000). A diode laser (650 nm, not shown) is used to align and balance the interferometer.

The dispersive samples are various combinations of SF6, SF57 and LLF1 glass rods [61]. Each new sample requires a displacement of mirrors M1 and M2, leading to different optical path lengths. For each sample, the pump

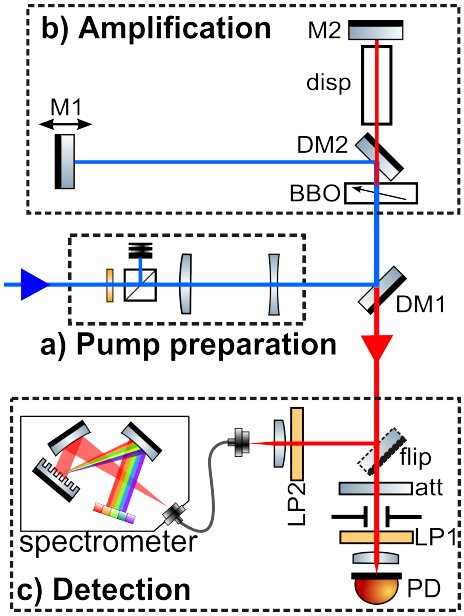

Figure 12: Experimental setup. a) An attenuator and a telescope are used to prepare the pump in power, polarization and diameter. b) PDC generated in the first pass of the pump in the BBO crystal is stretched temporally in a dispersive medium (disp) and sent back into the crystal to be amplified. The time of arrival of the pump is carefully tuned with the position of mirror M1, set on a translation stage. c) The PDC is sent into either a spectrometer or into a photodiode.

power is adjusted so that the amplified PDC does not saturate the spectrometer when the acquisition time is set to 5 µs. This way, the parametric gain is approximately equal for the different samples. Spectra are recorded as long as the interferometer yields stable and constructive interferograms. The frequency width is calculated by averaging the FWHM of every single spectrum. Alternatively, measurements of $g^{(2)}$ are made for the same pump power as for the spectra measurements; the number of acquired pulses is limited by the drifting time of the interferometer.

Experimental results are compared to theoretically predicted values based on the amplification of the Schmidt modes formalism. The behavior of the frequency spectral width and $g^{(2)}$ under different conditions, as well as the shape of the spectra, are examined. Theoretical predictions are performed with the parametric gain[3] $G = 7$, and by varying the argument of the $\cos[(\delta + \delta')/2]$ of the JSA of equation (60). In the experimental setup, those changes translate to a change in the configuration of the interferometer, namely the air thickness in both the PDC and the pump paths, as per the

[3]In the context of multimode radiation, the parametric gain is understood as the argument of the $\sinh^2$ of equation (51b) for the first Schmidt mode.

previous sections. Let us introduce a parameter that characterizes the *phase of the interferometer*, δ'_0, and which corresponds to the value of δ' at the center of the frequency spectrum (where $\lambda_s = \lambda_i = 800\,\text{nm}$). In the theoretical predictions, δ'_0 is varied from 0 to π with an increment of $\pi/8$. When $\delta'_0 = 0$, we get constructive interference in the center of the spectrum; when $\delta'_0 = \pi/2$, the interference is completely destructive. δ'_0 characterizes the phase of the interferometer because it depends only on the different media between the two nonlinear crystals.

Note that it is rather challenging to experimentally estimate the parametric gain, simply because it is defined for single-mode radiation. Furthermore, each sample corresponds to a slightly different setup (position of M1 and M2, pump power, length of the rods); therefore the distribution of the gain for each mode might vary for different configuration of the interferometer. The parametric gain used for theoretical predictions should be seen as an indication, and not a measured value nor a reference.

The frequency spectra obtained via simulations can be compared straightforwardly with experimental results. On the other hand, the experimental number of modes is obtained indirectly from the degree of second-order coherence with zero delay τ, following equation (70). From equation (14), in the case of single-mode degenerate collinear high-gain PDC, $g_1^{(2)} = 3$. $g^{(2)}$ is obtained experimentally from the approximation $g^{(2)}(\tau = 0) \approx \langle N^2 \rangle / \langle N \rangle^2$, where N is the intensity of the detected PDC, and where the approximation is valid when $N \gg 1$.

The raw wavelength spectra are multiplied by a factor of λ^4 according to the following argument [56]. The number of modes contained in the detection volume depends on the coherence volume of the PDC, which is wavelength dependant. Both the coherence area and the coherence time are proportional to λ^2. This means that, for higher wavelength, fewer modes —thus fewer photons—are collected by the pixels on the spectrometer's CCD array. This mismatch can be corrected by a factor proportional to λ^4.

4.4 Results and analysis

Introducing a strongly dispersive material between two nonlinear crystals has the effect of dramatically narrowing the frequency spectrum of parametric down conversion with respect to the spectrum of a single crystal, as well as amplifying the signal intensity of several orders of magnitude (figure 13). The spectrum varies a lot in time, both in amplitude and in shape (figure 14): the former can be readily explained by the defining strong intensity fluctuations of fields with $g^{(2)} > 1$; the latter is due to the sensitivity of

the spectrum shape to phase fluctuations between the pump and the PDC field. Each experimental spectrum in figure 14 results from a combination of both intensity and phase fluctuations over the 5 ms acquisition time, or 25 pulses. Fluctuations of the pump power were found to be negligible, with $g^{(2)} = 1.0000(4)$.

The phase fluctuations in the interferometer result in the averaging of the spectral density over the acquisition time. This can be seen by comparing various experimental spectra (figure 14) and theoretically predicted spectra (figure 15). In the experimental spectra, distinct features, such as one, two, or three peaks, can be identified. It appears that the same structures appear in the simulated spectra, where we go from one peak (constructive interference) to two peaks (destructive interference) and some intermediate structures, such as three peaks when the phase of the interferometer, δ_0', is $7\pi/8$.

The theoretically predicted effect of the phase on the frequency width and the intensity correlation shows that perfectly constructive interference ($\delta_0' = 0$) yields optimistic results, but not the best (figure 16). Accordingly, perfectly destructive interference is far from causing the broadest spectrum and the lowest $g^{(2)}$. The jumps in the frequency width are attributed to the evolving shape of the spectrum with the phase: when the height of the secondary peaks reach half the value of the central peak, the FWHM jumps accordingly.

Let us suppose perfectly random phase jumps in the interferometer so that PDC pulses follow a uniform probability distribution in δ_0'. Then, following figure 16, there is a higher probability that the pulse exhibit a $g^{(2)}$ closer to the lower boundary, since the "plateau" around $\delta_0' = \pi$ is much larger than the optimal peak around $\delta_0' = 0$. In other words, given that phase jumps are uniformly distributed, the number of modes will tend to be lower, in average, than the midway point between the optimistic and pessimistic scenarios.

As expected from high-gain simulations, and on par with the intuitive reasoning, the frequency spectrum of amplified PDC does get narrower as the amount of dispersion between the two crystals is increased (figure 17). The observed asymptotic trend culminates with an experimental spectral width of (1.22 ± 0.02) THz, corresponding to the sample with the largest GVD. The experimental results fit well between the theoretically allowed zone (pink in figure 17), which is obtained from different phase of the interferometer. As demonstrated before, there is partial averaging of the spectral density over the acquisition time of the pulses. The theoretical boundaries are simply determined by averaging the FWHM of different phase scenarios,

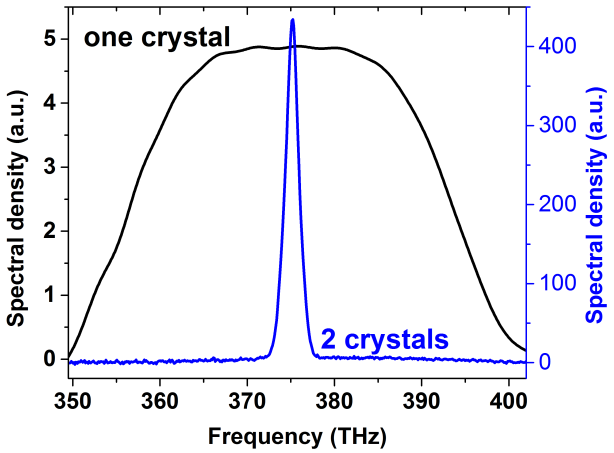

Figure 13: Experimental narrowing of the frequency spectrum of PDC using a dispersive medium between two crystals. The dispersive medium is a 19.4 cm rod of SF57, for a total length of 38.8 cm. The units of spectral density of each curve, albeit arbitrary, are the same, meaning that the narrow spectrum has a peak two orders of magnitude stronger than the broad spectrum.

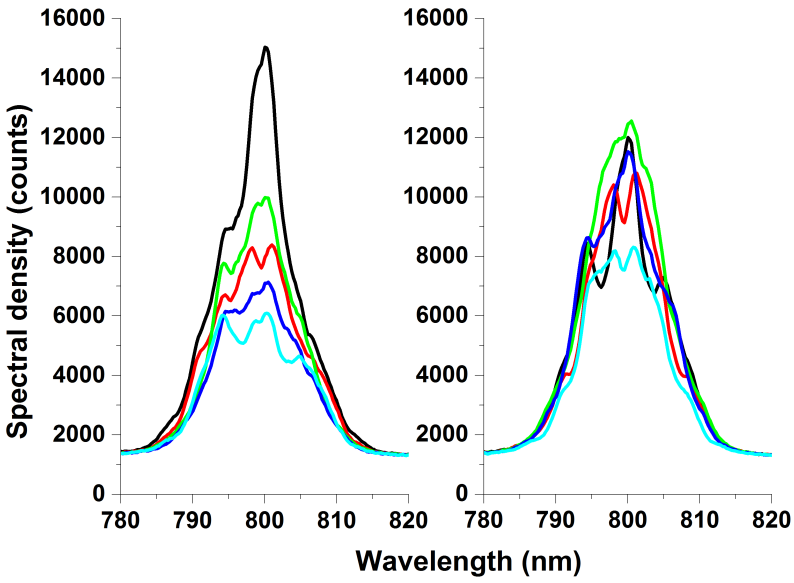

Figure 14: 2 sets of 5 consecutive spectra obtained experimentally with 17 cm of LLF1 (total of 34 cm of LLF1), corresponding to a GVD of 0.02448 ps^2. Acquisition time was 5 μs, so each spectrum corresponds to an average over 25 pulses.

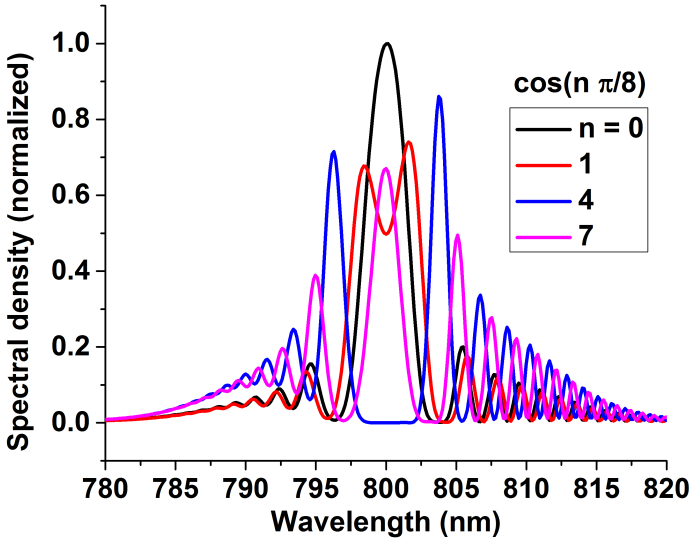

Figure 15: Theoretically predicted family of curves for 34 cm of LLF1, corresponding to 0.02448 ps^2 of GVD. The different curves correspond to different values of δ_0', and show how much the spectrum can be affected by the phase of the spectrometer. Parametric gain is 7.

and taking the area inside the standard deviation as an "allowed zone".

The number of modes, assessed through $g^{(2)}$, is reduced as well, until it reaches quasi-single mode radiation. The largest value of $g^{(2)}$ corresponds to the second-to-largest dispersion sample. One would have expected that the points in the right-hand part of figure 17, near the asymptote, exhibit single mode statistics. However, the contribution of the phase fluctuations in the interferometer, as well as non optimized configurations of the interferometer, has a significant impact on the number of modes. Note that, in general, intensity fluctuations will artificially increase the value of intensity autocorrelation. This effect was not considered here.

Background PDC—the PDC signal that is not amplified in the second crystal, highly multimode in nature—might also have a non negligible contribution on $g^{(2)}$. Each interface of the dispersive samples, which are uncoated, sends background PDC into the diode. As a simple test, we put an interference filter ($\Delta\lambda = 10\,\mathrm{nm}$) in front of the detector to cut part of the background PDC, and $g^{(2)}$ immediately went from 2.05 ± 0.01 to 2.29 ± 0.02. Another cause for $g^{(2)}$ not reaching 3 might be the presence of several angular modes. However, a pinhole, whose aperture size is set smaller than

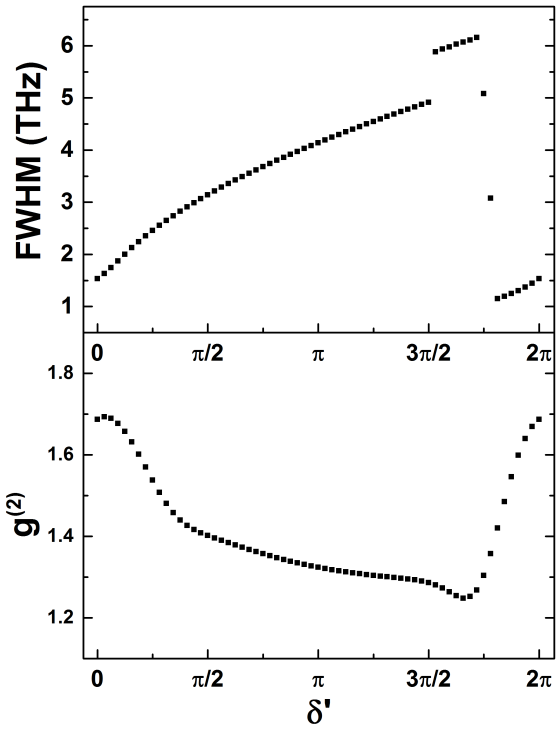

Figure 16: Theoretically predicted FWHM and $g^{(2)}$ dependence on the phase of the interferometer δ_0', with a 34 cm sample of LLF1 (GVD of 0.02448 ps^2) and a parametric gain of 7.

the estimated first angular mode [17], was set in the detector's arm for this specific purpose.

A gain of 7, even in the optimistic scenario of constructive interference, and assuming no stray light, does not yield single-mode radiation. In figure 18, we see that the maximum value of $g^{(2)}$ increases with the parametric gain. A higher gain will yield a higher $g^{(2)}$, until the maximal value of 3 is reached. With a parametric gain of 10, which is experimentally feasible, the value of $g^{(2)}$ reaches a maximum of 2.89, which corresponds to 1.06 frequency mode. From this, we can conclude that it is possible, with a perfectly stabilized interferometer in a configuration for constructive interference and a parametric gain of approximately 10, to generate frequency single-mode PDC.

Varying the time of arrival of the pump pulse with respect to the PDC pulse has the effect of generating two peaks on either side of the degenerate

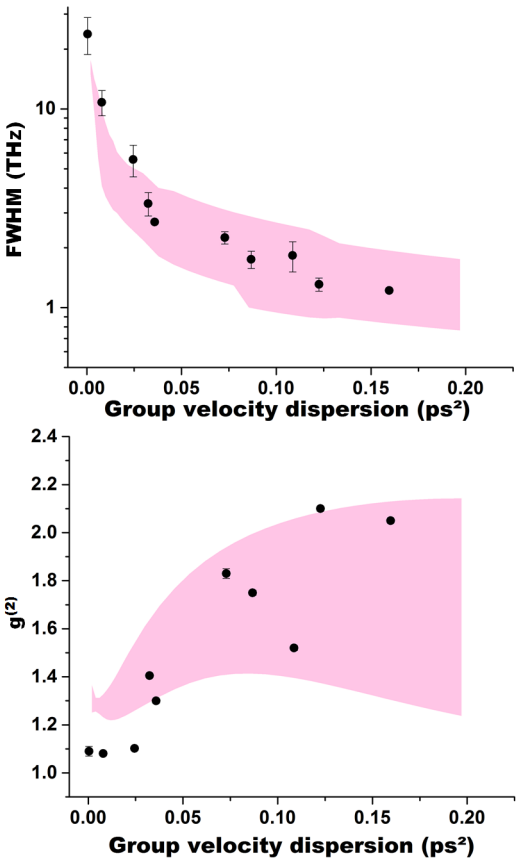

Figure 17: FWHM and $g^{(2)}$ dependence on the amount of dispersion in the medium between the crystals. Experimental points (black) are compared to theoretically predicted values (pink zone). Theoretical predictions were obtained by averaging the FWHM and the $g^{(2)}$ of the 8 simulated curves; the pink zone is delimited by the standard deviations. The experimental FWHM points were obtained by averaging the FWHM of M consecutive spectra, each obtained with an acquisition time of 5 or 10 µs (25 or 50 pulses). Experimental $g^{(2)}$ points were obtained by measuring $\langle N^2 \rangle / \langle N \rangle^2$. The number of spectra M and the acquisition time of $g^{(2)}$ were limited by the drifting time of the interferometer.

frequency, equally apart therefrom, and of equal amplitude, both experimentally and from theoretical predictions (figure 19). From theory, this can be understood from energy conservation, $\omega_p = \omega_s + \omega_i$. A longer time of arrival mismatch induces stronger detuning from degeneracy and weaker PDC intensity, until the two peaks completely fade out. The observed intensity fluctuations are larger at degeneracy than in the two-color case. This is because each channel of two-mode squeezed vacuum is known to exhibit thermal statistics, whereas single-mode squeezed vacuum fluctuates more, with $g^{(2)} = 3$. In the two-color case, unlike what was obserbed in the degen-

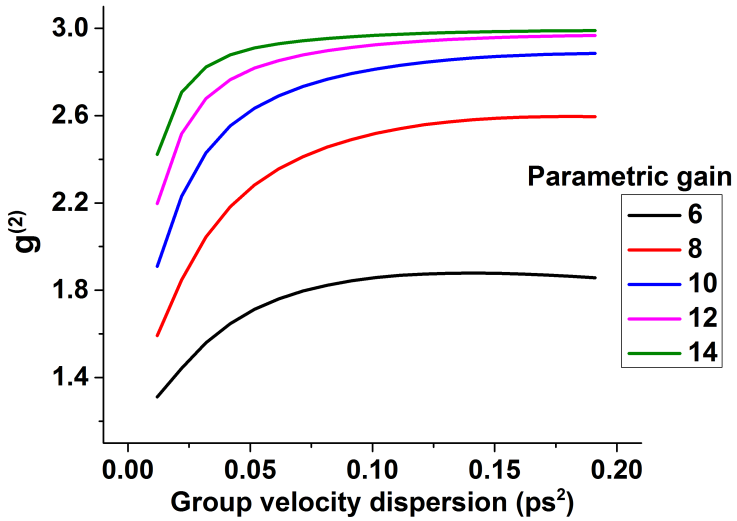

Figure 18: Theoretically predicted $g^{(2)}$ vs group velocity dispersion for different values of the parametric gain. Only constructive interference is considered ($\delta_0' = 0$).

erate case, the spectrum was not prone to significant shape modifications upon phase fluctuations, both experimentally and from theoretical predictions.

The position of the peaks do not quite match: the predicted peaks are slightly further apart than the experimental peaks (figure 19). This can be attributed to the difficulty of experimentally pinpointing the position for degeneracy. Upon displacing the pump mirror across the position of degeneracy, the spectrum goes from 2 peaks, which merge into one highly fluctuating peak, and split back again into two peaks. The "one-peak" zone is large, at about 0.1 mm, and it is sufficient to explain the position mismatch between the experimental and the theoretically predicted spectra.

4.5 Conclusion

In conclusion, a filterless and narrowband amplification of PDC was demonstrated by inserting a dispersive medium between two OPAs operated in the high-gain regime. The sample with the strongest group velocity dispersion exhibited a spectral width of (1.22±0.02) THz, a spectacular narrowing from the spectrum of a single crystal, at (36.7±0.1) THz. Meanwhile, the number of modes was reduced down to 1.82±0.02. The theoretical predictions accurately fit the experimental results, but only when different phases of the interferometer are taken into account. Similarly, the predicted number of modes was very sensitive to those fluctuations. Only with a very high

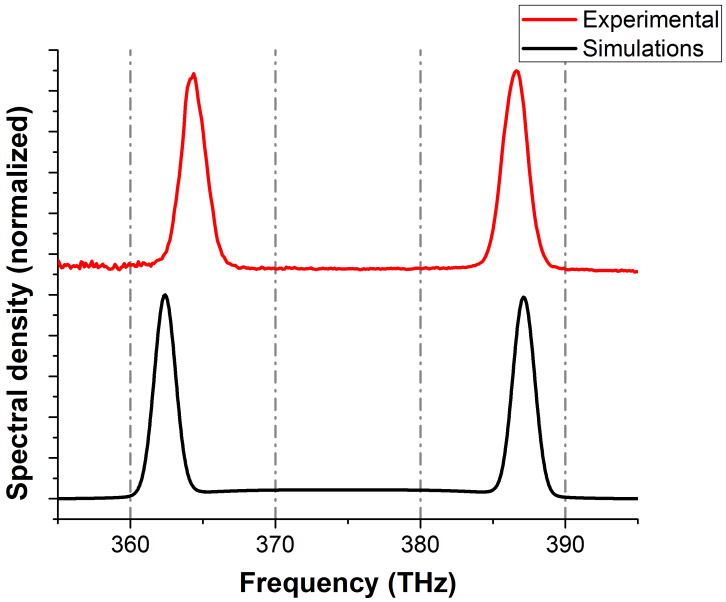

Figure 19: Experimental results (top) and theoretical predictions (bottom) for the two-color case with an additional (1.60±0.01) mm-thick layer of air in the pump path, from the degenerate case. The parametric gain for theoretical predictions is 8.3.

gain and a stabilized phase did the simulations yield single-mode radiation. Alternatively, the separation method shown in chapter 3 was not as sensitive to phase jumps, since the three waves were travelling together.

By varying the time of arrival of the pump pulse, the source can be used to generate and tune bright narrowband two-color PDC without varying the angle of the crystal. Predictions based on the provided theory were again successful to fit experimental results.

The method presented in this section brings us closer to single-mode bright squeezed vacuum states of light, and could in principle be combined with single angular mode selection methods. Selection of a single angular mode was demonstrated before by using the crystals separation method [45]. The success of this method relies on the tightness of the pump spatial profile, as well as on the distance between the crystals; the temporal mode selection method presented here depends on the pump pulse duration and on the amount of GVD in the medium inserted between the crystals. Those quantities are compatible and could lead to the generation of single-mode BSV. The combination was experimentally tested, but is at an early stage and requires further investigation. Mainly, the sensitivity of the spectrum

to phase jumps will be addressed.

Throughout this section, the predictions, as well as the intuition, were based on the Schmidt mode formalism. The Schmidt mode formalism provides complete information about the PDC biphoton field in the high-gain regime, included the frequency spectrum and the number of modes. The number of modes can be used to compute the intensity autocorrelation $g^{(2)}$, which can be compared straightforwardly to experimental results. The theoretical predictions based on the Schmidt mode formalism were surprisingly accurate, especially in predicting the width of the spectra. The theory could also provide information about the different amplification eigenmodes: their spectral shape, width, and relative weight provide useful information about the nature of high-gain PDC.

5 Conclusion

Bright squeezed vacuum states of light (BSV) are typically generated by strongly pumping a nonlinear crystal, making them highly multimode in nature, both in angle and in frequency. The ultimate goal of the work presented in this thesis is the generation of single-mode bright squeezed vacuum states of light (BSV) in order to benefit from their nonclassical properties. The crystal-separation method was found to produce single-mode PDC in the angles. It was demonstrated that single angular mode PDC exhibited twin-beam squeezing in the form of noise reduction in the photon number difference. The introduction of a highly dispersive medium between the two strongly pumped nonlinear crystals had the effect of reducing the narrowing the frequency spectrum down to quasi single-mode radiation in frequency. The theoretical framework was based on the Schmidt mode decomposition of the parametric amplification process.

When the distance between two strongly pumped travelling wave OPAs is increased, the number of angular modes gets smaller and smaller, until it reaches quasi single-mode radiation. This happens because the PDC generated in the first crystal has a much wider angular spectral width than the divergence of the pump, resulting in a selective amplification in the angles. This can be easily seen from a geometrical picture, where the overlap between the pump and the PDC in the second crystal depends on the separation distance between the crystals. The number of angular modes could be reduced down to 1.13 ± 0.06.

Twin-beam squeezing can be experimentally tested via the noise reduction factor (NRF), which is the variance of the photon number difference between the two PDC channels normalized over the total number of photons, so that NRF $= 1$ corresponds to the shot-noise limit, and NRF < 1 is a sufficient sign for twin-beam squeezing, with a minimum boundary at zero. An idealized measure of the NRF with squeezed vacuum would yield NRF $= 0$, since all photons are created in pairs. However, the NRF inevitably increases due to the imperfect quantum efficiency of the detectors. Also, any effect that causes one photon from a pair to be detected, but not its twin, causes the NRF to increase as well. The magnitude of this effect increases with the total number of photons, making squeezing more sensitive to unmatched mode in the high-gain regime. The crystals separation method was devised to generate bright single-mode PDC in the angles. In this thesis, it was shown that PDC generated from the crystals separation method exhibited twin-beam squeezing as well, with NRF $= 0.683 \pm 0.004$ for the single angular mode case. When the distance between the nonlinear crystals is varied, modulations in the NRF are observed, which are due to interference effects between the two crystals. When there is construc-

tive interference, the number of photons is high, thus the NRF reaches a maximum. To summarize, it was shown that the single angular mode PDC produced by the crystal separation method exhibits twin-beam squeezing, but the NRF was not optimally low due to the presence of unmatched modes.

The PDC generated from a single crystal is so broad that a NRF measurement hardly beat the shot-noise level due the presence of many unmatched modes, without the use of mode-matching apertures to mitigate the effects of imperfect alignment of the experimental setup and of asymmetric optical components. In this thesis, fair twin-beam squeezing was observed without the use of mode-matching apertures. This directionality of the squeezing, since most of the photons are contained in a single angular mode, adds to the versatility of squeezed states, and could have significant impact in the field of quantum information.

Imposing group velocity dispersion on a PDC pulse between two OPAs had the effect to stretch the PDC pulse in time and chirp it, so that frequency and time were correlated. The intense and short pump pulse could then be used to selectively amplify a narrower frequency band of the PDC in the second OPA, thereby reducing the number of modes. The rest of the PDC from the first OPA is negligible because the parametric amplification is exponentional in the high-gain. A spectral width of (1.22±0.02) THz was demonstrated, a substantial narrowing from the spectrum of a single crystal, at (36.7±0.1) THz. Meanwhile, the number of modes went from approximately a hundred with a single crystal to 1.82±0.02 with the 2 crystals and the dispersive medium. Two OPAs with a tunable phase between them form a nonlinear interfometer. It was found that the phase relation between the three channels (pump, signal and idler) can have a strong effect on the number of modes and frequency spectral width. Furthermore, the nonlinear interferometer was found to be extremely sensitive to phase fluctuations. The effects of the phase was theoretically simulated and corroborated by experimental results. The parametric gain has a strong influence in the efficiency of the mode selection method. In a hypothetical perfectly stabilized nonlinear interferometer, a gain of 10 (experimentally feasible) would be sufficient to generate single mode PDC in the frequencies.

The two main experiments presented in this thesis demonstrated the following:

i Reduction of the number of angular modes by using the nonlinear crystals separation method;

ii Twin-beam squeezing from single angular mode PDC; and

iii Reduction of the number of frequency modes by introducing a dispersive

medium between two nonlinear crystals.

Those two steps are of significant importance in our goal to generate truly single-mode BSV. The two methods for mode selection, one for the frequencies and the other for the angles, are in principle compatible: the efficiency of the first one depends on the pump pulse duration and the amount of dispersion in the PDC arm; the efficiency of the second one depends on the tightness of the pump's spatial profile and the distance between the two crystals [46]. At the moment of writing this text, the combination of the methods was not successful. Many causes will be considered, such as an insufficiently tight pump profile or an inadequate configuration of the interferometer resulting in destructive interference and increasing the number of modes. Even though the number of modes obtained with the frequency mode filtering method did not quite reach one, the source can still be used for some applications such as phase supersensitivity in nonlinear interferometers with a macroscopic beam, or upconversion of BSV.

The Schmidt mode formalism used throughout this thesis opens the door to whole new world of possibilities for quantum information. The rich modal structure in the frequencies and the angles can be used to encode quantum information in a countably infinite basis, corresponding to the amplification eigenmodes. Furthermore, polarization entanglement between two macroscopic beams was observed as well, pushing further the variety of macroscopic quantum effects [62].

References

[1] M. O. Scully and M. S. Zubairy. *Quantum optics*. Cambridge University Press, 1997.

[2] A. I. Lvovsky. Squeezed light. *Photonics, Volume 1: Fundamentals of Photonics and Physics*, 1, 2015.

[3] I. N. Agafonov, M. V. Chekhova, and G. Leuchs. Two-color bright squeezed vacuum. *Phys. Rev. A Vol. 82*, 2010.

[4] M. Bondani, A. Allevi, G. Zambra, M. G. A. Paris, and A. Andreoni. Sub-shot-noise photon-number correlation in a mesoscopic twin beam of light. *Phys. Rev. A Vol. 76*, 2007.

[5] T. Sh. Iskhakov, A. M. Pérez, K. Yu Spasibko, M. V. Chekhova, and G. Leuchs. Superbunched bright squeezed vacuum state. *Optics Letters*, 37(11):1919–1921, 2012.

[6] M. V. Chekhova, G. Leuchs, and M. Żukowski. Bright squeezed vacuum: Entanglement of macroscopic light beams. *Optics Communications*, 337:27–43, 2015.

[7] G. Brida, M. Genovese, and I. Ruo Berchera. Experimental realization of sub-shot-noise quantum imaging. *Nature Photonics*, 4(4):227–230, 2010.

[8] E. D. Lopaeva, I. Ruo Berchera, I. P. Degiovanni, S. Olivares, G. Brida, and M. Genovese. Experimental realization of quantum illumination. *Physical Review Letters*, 110(15):153603, 2013.

[9] G. Brida, I. P. Degiovanni, M. Genovese, M. L. Rastello, and I. Ruo Berchera. Detection of multimode spatial correlation in pdc and application to the absolute calibration of a ccd camera. *Optics Express*, 18(20):20572–20584, 2010.

[10] F. Hudelist, Kong J., C. Liu, J. Jing, Z.Y. Ou, and W. Zhang. Quantum metrology with parametric amplifier-based photon correlation interferometers. *Nat. Comm 5, Article 3049*, 2014.

[11] O. Jedrkiewicz, J.-L. Blanchet, A. Gatti, E. Brambilla, and P. Di Trapani. High visibility pump reconstruction via ultra broadband sum frequency mixing of intense phase-conjugated twin beams. *Optics Express*, 19(14):12903–12912, 2011.

[12] I. Abram, R. K. Raj, J.-L. Oudar, and G. Dolique. Direct observation of the second-order coherence of parametrically generated light. *Physical Review Letters*, 57(20):2516, 1986.

[13] A. M. Pérez, F. Just, A. Cavanna, M. V. Chekhova, and G. Leuchs. Compensation of anisotropy effects in a nonlinear crystal for squeezed vacuum generation. *Laser Physics Letters*, 10(12):125201, 2013.

[14] B. Yurke, S. L. McCall, and J. R. Klauder. SU(2) and SU(1,1) interferometers. *Phys. Rev. A Vol. 33, Issue 6*, page 4033, 1986.

[15] Z. Y. Ou. Enhancement of the phase-measurement sensitivity beyond the standard quantum limit by a nonlinear interferometer. *Physical Review A*, 85(2):023815, 2012.

[16] W. N. Plick, J. P. Dowling, and G. S Agarwal. Coherent-light-boosted, sub-shot noise, quantum interferometry. *New Journal of Physics*, 12(8):083014, 2010.

[17] W. Wasilewski, A. I. Lvovsky, K. Banaszek, and C. Radzewicz. Pulsed squeezed light: Simultaneous squeezing of multiple modes. *Phys. Rev. A Vol. 73, 063819*, 2006.

[18] C. K. Law and J. H. Eberly. Analysis and interpretation of high transverse entanglement in optical parametric down conversion. *Phys. Rev. Lett. Vol. 92, 127903*, 2004.

[19] Yu M. Mikhailova, P. A. Volkov, and M. V. Fedorov. Biphoton wave packets in parametric down-conversion: Spectral and temporal structure and degree of entanglement. *Physical Review A*, 78(6):062327, 2008.

[20] A. Eckstein, A. Christ, P. J. Mosley, and C. Silberhorn. Highly efficient single-pass source of pulsed single-mode twin beams of light. *Physical Review Letters*, 106(1):013603, 2011.

[21] P. Sharapova, A. M. Pérez, O. V. Tikhonova, and M. V. Chekhova. Schmidt modes in the angular spectrum of bright squeezed vacuum. *Phys. Rev. A 91, 043816*, 2015.

[22] D. F. Walls and G. J. Milburn. *Quantum optics*. Springer Science & Business Media, 2007.

[23] O. Jedrkiewicz, Y.-K Jiang, E. Brambilla, A. Gatti, M. Bache, L. A. Lugiato, and P. Di Trapani. Detection of sub-shot-noise spatial correlation in high-gain parametric down conversion. *Phys. Rev. Lett. Vol. 93*, page 243601, 2004.

[24] P. J. Mosley, J. S. Lundeen, B. J. Smith, P. Wasylczyk, A. B. U'Ren, C. Silberhorn, and I. A. Walmsley. Heralded generation of ultrafast single photons in pure quantum states. *Phys. Rev. Lett. Vol. 100*, 2008.

[25] D. N. Klyshko. Ramsey interference in two-photon parametric scattering. *Zh. Eksp. Teor. Fiz. Vol. 104*, pages 2676–2684, 1993.

[26] P. A. M. Dirac. The quantum theory of the emission and absorption of radiation. *Proc. R. Soc. Lond. A Vol. 114*, pages 243–265, 1927.

[27] R. J. Glauber. The quantum theory of optical coherence. *Phys. Rev. Vol. 130*, pages 2529–2539, 1963.

[28] R. J. Glauber. Coherent and incoherent states of the radiation field. *Phys. Rev. Vol. 131*, pages 2766–2788, 1963.

[29] J. S. Bell. On the Einstein Podolsky Rosen paradox. *Physics Vol. 1, Issue 3*, 1964.

[30] T. Herbst, T. Scheidl, M. Fink, J. Handsteiner, B. Wittmann, R. Ursin, and A. Zeilinger. Teleportation of entanglement over 143 km. *PNAS*, 112(14):14202–14205.

[31] R. P. Feynman. Simulating physics with computers. *Intern. Journ. of Theor. Phys. Vol. 21, Issue 6*, pages 467–488, 1982.

[32] P. W. Shor. Algorithms for quantum computation: discrete logarithms and factoring. *Proc. 35th Annu. Symp. on the Foundations of Computer Science*, pages 124–134, 1994.

[33] A. K. Ekert. Quantum cryptography based on Bell's theorem. *Physical Review Letters*, 67(6):661, 1991.

[34] S. L. Braunstein and A. K. Pati. *Quantum information with continuous variables*. Springer Science & Business Media, 2012.

[35] T. C. Ralph. Continuous variable quantum cryptography. *Physical Review A*, 61(1):010303, 1999.

[36] D Stoler. Equivalence classes of minimum uncertainty packets. *Phys. Rev. D. Vol. 1, Issue 12*, 1970.

[37] H. P. Yuen and J. H. Shapiro. Optical communication with two-photon coherent states–part i: Quantum-state propagation and quantum-noise. *IEEE Trans. Inf. Theory Vol. IT-24*, 1978.

[38] H. P. Yuen and J. H. Shapiro. Optical communication with two-photon coherent states–part ii: Photoemissive detection and structured receiver performance. *IEEE Trans. Inf. Theory Vol. IT-25*, 1979.

[39] H. P. Yuen and J. H. Shapiro. Optical communication with two-photon coherent states–part iii: Quantum measurements realizable with photoemissive detectors. *IEEE Trans. Inf. Theory Vol. IT-26*, 1980.

[40] C. M. Caves. Quantum-mechanical noise in an interferometer. *Phys. Rev. D Vol. 23, Issue 8*, 1981.

[41] R. E. Slusher, L. W. Hollberg, B. Yurke, J. C. Mertz, and J. F. Valley. Observation of squeezed states generated by four-wave mixing in an optical cavity. *Phys. Rev. Lett. Vol. 55*, 1985.

[42] L.-A. Wu, J. Kimble, J. L. Hall, and H. Wu. Generation of squeezed states by parametric down conversion. *Phys. Rev. Lett. Vol. 57*, 1986.

[43] A. I. Lvovsky and M. G. Raymer. Continuous-variable optical quantum-state tomography. *Reviews of Modern Physics*, 81(1):299, 2009.

[44] H. Hansen, T. Aichele, C. Hettich, P. Lodahl, A. I. Lvovsky, J. Mlynek, and S. Schiller. Ultrasensitive pulsed, balanced homodyne detector: application to time-domain quantum measurements. *Optics Letters*, 26(21):1714–1716, 2001.

[45] A. M. Pérez, T. Sh. Iskhakov, P. Sharapova, S. Lemieux, O. V. Tikhonova, M. V. Chekhova, and G. Leuchs. Bright squeezed-vacuum source with 1.1 spatial mode. *Optics Letters Vol. 39, Issue 8*, pages 2403–2406, 2014.

[46] T. Sh. Iskhakov, S. Lemieux, A. M. Pérez, R. W. Boyd, M. V. Chekhova, and G. Leuchs. Nonlinear interferometer for tailoring the frequency spectrum of bright squeezed vacuum. *Journal of Modern Optics*, pages 1–7, 2015.

[47] G. Grynberg, A. Aspect, and C. Fabre. *Introduction to quantum optics: from the semi-classical approach to quantized light*. Cambridge University Press, 2010.

[48] R. Loudon. *The quantum theory of light*. Oxford University Press, 2000.

[49] Robert W Boyd. *Nonlinear optics*. Academic press, 2003.

[50] B. E. A. Saleh and M. C. Teich. *Fundamentals of photonics*, volume 22. Wiley New York, 1991.

[51] D. Eimerl, L. Davis, S. Velsko, E. K. Graham, and A. Zalkin. Optical, mechanical, and thermal properties of barium borate. *Journal of applied physics*, 62(5):1968–1983, 1987.

[52] F. M. Miatto, T. Brougham, and A. M. Yao. Cartesian and polar schmidt bases for down-converted photons. *Eur. Phys. J. D Vol. 66, Issue 183*, 2012.

[53] C. H. Monken, P. H. S. Ribeiro, and S. Pádua. Transfer of angular spectrum and image formation in spontaneous parametric down-conversion. *Physical Review A*, 57(4):3123, 1998.

[54] W. P. Grice and I. A. Walmsley. Spectral information and distinguishability in type-ii down-conversion with a broadband pump. *Physical Review A*, 56(2):1627, 1997.

[55] Yu. M. Mikhailova, P. A. Volkov, and M. V. Fedorov. Biphoton wave packets in parametric down-conversion: Spectral and temporal structure and degree of entanglement. *Phys. Rev. A Vol. 78, 062327*, 2008.

[56] K. Yu. Spasibko, T. Sh. Iskhakov, and M. V. Chekhova. Spectral properties of high-gain parametric down-conversion. *Optics Exp. Vol. 20, Issue 7*, pages 7507–7515, 2012.

[57] A. B. URen, R. K. Erdmann, M. de La Cruz-Gutierrez, and I. A. Walmsley. Generation of two-photon states with an arbitrary degree of entanglement via nonlinear crystal superlattices. *Physical Review Letters*, 97(22):223602, 2006.

[58] G. Brida, L. Caspani, A. Gatti, M. Genovese, A. Meda, and I. R. Berchera. Measurement of sub-shot-noise spatial correlations without background subtraction. *Phys. Rev. Lett. Vol. 102*, 2009.

[59] O. A. Ivanova, T. Sh. Iskhakov, A. N. Penin, and M. V. Chekhova. Multiphoton correlations in parametric down-conversion and their measurement in the pulsed regime. *Quantum Electron. Vol. 36 Num. 10*, page 951, 2006.

[60] T. Sh. Iskhakov, M. V. Chekhova, and G. Leuchs. Generation and direct detection of broadband mesoscopic polarization-squeezed vacuum. *Physical Review Letters*, 102(18):183602, 2009.

[61] SCHOTT optical glass data sheets 2012-12-04.

[62] T. Sh. Iskhakov, I. N. Agafonov, M. V. Chekhova, and G. Leuchs. Polarization-entangled light pulses of 10^5 photons. *Phys. Rev. A Vol. 33, Issue 6*, page 4033, 1986.